Centennial- and orbital-scale erosion beneath the Greenland Ice Sheet

A. Balter-Kennedy[1,2], N.E. Young[1], J.P. Briner[3], B.L. Graham[3], J.M. Schaefer[1,2]

[1]Lamont-Doherty Earth Observatory, Columbia University, Palisades, New York, USA,

[2]Department of Earth and Environmental Sciences, Columbia University, New York, New York, USA, [3]Department of Geology, University at Buffalo, Buffalo, New York, USA

Corresponding author: Allie Balter-Kennedy (abalter@ldeo.columbia.edu)

Key points

- Centennial-scale erosion rates near Jakobshavn Isbræ were 0.4–0.8 mm yr^{-1}.
- Orbital-scale erosion rates derived from a ^{10}Be depth profile in a bedrock core were 0.1–0.3 mm yr^{-1}.
- Erosion rates beneath the Greenland Ice Sheet near Jakobshavn Isbræ remained relatively constant through the Pleistocene.

Abstract

Erosion beneath glaciers and ice sheets is a fundamental Earth-surface process dictating landscape development, which in turn influences ice-flow dynamics and the climate sensitivity of ice masses. The rate at which subglacial erosion takes place, however, is notoriously difficult to observe because it occurs beneath modern glaciers in a largely inaccessible environment. Here, we present 1) cosmogenic-nuclide measurements from bedrock surfaces with well constrained exposure and burial histories fronting Jakobshavn Isbræ in western Greenland to constrain centennial-scale erosion rates, and 2) a new method combining cosmogenic nuclide measurements in a shallow bedrock core with cosmogenic-nuclide modelling to constrain orbital-scale erosion rates across the same landscape. Twenty-six ^{10}Be measurements in surficial bedrock constrain the erosion rate during historical times to 0.4–0.8 mm yr^{-1}. Seventeen ^{10}Be measurements in a 4-m-long bedrock core corroborate this centennial-scale erosion rate, and reveal that ^{10}Be concentrations below ~2 m depth are greater than what is predicted by an idealized production-rate depth profile. We utilize this excess ^{10}Be at depth to constrain orbital-scale erosion rates at Jakobshavn Isbræ to 0.1–0.3 mm yr^{-1}. The broad similarity between centennial- and orbital-scale erosion rates suggests that subglacial erosion rates have remained relatively uniform throughout the Pleistocene at Jakobshavn Isbræ.

Plain Language Summary

Glaciers and ice sheets are among the most powerful erosional forces on Earth, with the ability to alter topography and cut deep valleys into the landscape on relatively short timescales. The total amount of erosion and the pace at which it takes place affects how the glaciers flow and how they respond to climate changes. The pace of erosion beneath glaciers, however, is difficult to measure because it takes place in an environment that is difficult to access. Here, we use cosmogenic-nuclide analyses, which are specialized chemical measurements in rock that tell us how long the rock has been exposed at the Earth's surface (in other words, how long the rock has been ice-free). These measurements also allow us to learn about the pace of erosion beneath the Greenland Ice Sheet over the Pleistocene epoch, which spans the last ~2.7 million years when the Earth experienced repeated ice ages. We find that the pace of erosion beneath the Greenland Ice Sheet has remained relatively consistent over the Pleistocene, a finding that helps us understand how the topography of Greenland has evolved through time.

1 Introduction

Subglacial erosion and sediment transport drive landscape evolution in mountainous regions and the mid-to-high latitudes (Brocklehurst & Whipple, 2004; Brozović, 1997). These processes reshape topography at the glacier bed, altering ice flow dynamics and the climate sensitivity of an ice mass (Egholm et al., 2017; Kessler et al., 2008; Pedersen et al., 2014; Pedersen & Egholm, 2013). Understanding the rate at which subglacial erosion takes place is critical for reconstructing past, and projecting future, ice-sheet volumes under different climate forcings (Lowry et al., 2020; Wilson et al., 2012). For example, numerical ice-sheet models used to simulate past and future ice-sheet evolution typically rely on a basal sliding parameter that is sparsely constrained by empirical measurements (e.g., Cuzzone et al., 2018; Larour et al., 2012; Morlighem et al., 2010). Despite the importance of including basal processes in ice sheet models, comparatively less focus has been placed on measuring erosion rates beneath ice sheets than alpine glacier systems (e.g., Cook et al., 2020; Herman et al., 2021; Koppes et al., 2015) The Greenland Ice Sheet (GrIS) is of particular concern, as it exhibits sustained mass loss in response to modern warming (King et al., 2020), yet the rate at which subglacial erosion and sediment transport takes place beneath the ice sheet remains poorly constrained.

Basal sliding, ice flux, effective pressure at the bed, and the erosivity of the bedrock (i.e., lithology) control subglacial abrasion and quarrying rates (Alley et al., 2019; Boulton, 1996; Hallet et al., 1996), yet empirical measurement of these processes is notoriously challenging given that they take place beneath ice. Except for a few *in situ* measurements of contemporary subglacial erosion (Boulton, 1979; Cohen et al., 2005), most estimates of glacial erosion rely on sediment flux through proglacial rivers (modern timescales; e.g., Cowton et al., 2012), sediment volumes in proglacial depocenters (centennial-to-millennial timescales) (e.g., Koppes & Montgomery, 2009), or denudation rates from thermochronometry (millions of years) (e.g., Herman et al., 2013). These methods are crucial for constraining subglacial erosion rates, but they often cannot elucidate spatial patterns of erosional processes within a glacier catchment and, on longer timescales, are averages of times when erosion is rapid, slowed, or even absent (Ganti et al., 2016). Cosmogenic-nuclide measurements from bedrock eroded subglacially offer an opportunity to capture spatial and temporal variability and provide empirical targets for glaciological models.

Production of cosmogenic nuclides in bedrock takes place only when the rock is ice-free and decreases exponentially with depth from the surface (e.g., Brown et al., 1992; Lal, 1991); subglacial erosion removes bedrock to a depth determined by the erosion rate and the duration of ice cover, beginning with the upper surfaces of the rock with the highest cosmogenic-nuclide inventory. Therefore, cosmogenic nuclide concentrations in bedrock hold information about the exposure history and amount of subglacial erosion experienced at a given location (Balco et al., 2014; Bierman et al., 1999; Briner & Swanson, 1998; Fabel et al., 2004; Goehring et al., 2011; Harbor et al., 2006; Hippe, 2017; Knudsen et al., 2015; Young et al., 2016, 2021). For example, ^{10}Be and ^{26}Al concentrations from sub-ice bedrock at the GISP2 site in central Greenland constrain likely exposure, burial, and erosional histories at that site through the Pleistocene (Schaefer et al., 2016). While accumulation of cosmogenic nuclides at the GISP2 site represents an extreme endmember, possible only when Greenland is nearly ice-free, the margins of the GrIS are retreating rapidly in response to modern warming (King et al., 2020), revealing a bedrock landscape whose cosmogenic-nuclide inventory holds yet-untapped information about exposure history and importantly, subglacial erosion rates during past periods of ice cover (Goehring et al., 2011; Pendleton et al., 2019; Rand & Goehring, 2019; Skov et al., 2020; Strunk et al., 2017; Young et al., 2021).

Using the well constrained Holocene exposure history for bedrock fronting the GrIS in the Jakobshavn Isbræ (Sermeq Kujalleq) forefield, Young et al. (2016) quantified subglacial erosion rates at eight locations covered by ice in the late Holocene. Here, we first build upon the dataset of Young et al. (2016) by calculating centennial-scale subglacial erosion rates in the Jakobshavn Isbræ region from new bedrock locations uncovered by the retreating GrIS within the last few decades. With these data, we evaluate spatiotemporal patterns of subglacial erosion and sediment evacuation during the period of historical ice cover. In addition, we present a cosmogenic ^{10}Be depth profile in a 4-m-long bedrock core from the same landscape, which we use to corroborate the erosion rates obtained from our surficial bedrock samples. Using this ^{10}Be depth profile as a case study, we detail a novel approach to quantifying subglacial erosion rates on orbital timescales using muon-produced ^{10}Be inherited from previous Pleistocene interglacials. Combined, these methods allow us to quantify *in situ* centennial- and orbital-scale subglacial erosion rates in the same location, opening new opportunities for estimating the rate of landscape development from bedrock in proglacial and subglacial environments.

2 Setting and ice-margin history

Jakobshavn Isfjord is a narrow fjord (5–10 km wide) that extends ~50 km from Disko Bugt to the GrIS margin at Jakobshavn Isbræ, a large outlet glacier that drains ~7% of the GrIS (Fig. 1; Joughin et al., 2004). Between Disko Bugt and Jakobshavn Isbræ, the ice-free landscape is characterized by glacially-scoured, striated crystalline bedrock of generally uniform lithology (gneiss) overlain by erratic boulders and sporadic patches of drift (Weidick, 1968; Weidick & Bennike, 2007; Young et al., 2011). A fresh glacier trimline extends ~2–4 km outboard of the modern terrestrial ice margin, delineated by the so-called “historical moraine” (Figure 1), which marks the maximum late Holocene extent of Jakobshavn Isbræ ~1850 CE (Weidick et al., 1990; Weidick & Bennike, 2007).

The ice-margin history at Jakobshavn Isbræ through the Holocene is well documented. ^{10}Be ages near the mouth of Jakobshavn Isfjord reveal that ice retreated out of Disko Bugt and onto land just prior to ~10 ka. This was followed by brief readvances of the ice margin near the fjord mouth at ca. 9.2 and 8.2 ka (Young et al., 2013b) and to within the historical limit, and likely behind the modern terminus, by 7520 ± 170 ka (Young et al., 2011). Through the Holocene Thermal Maximum (HTM; ~8–5 ka), when local summer temperatures were likely ~2–3 °C warmer than today in the Jakobshavn Isfjord region (Axford et al., 2013), Jakobshavn Isbræ continued to retreat inland, reaching a minimum extent after peak HTM warmth. Sedimentary sequences from proglacial-threshold lakes constrain the timing of the minimum GrIS position during the Holocene (Briner et al., 2010). When the glacier terminus is within the catchment of a threshold lake, but not overriding the lake, the lake receives silt-laden meltwater from the GrIS; when ice retreats out of the lake’s catchment, meltwater influx ceases and organic sedimentation dominates. Radiocarbon-dated material at the contact between organic matter and minerogenic layers provides limiting ages on the GrIS' withdrawal from, or advance into, a lake's basin. Minimum-limiting radiocarbon ages from South Oval Lake and Eqaluit Taserssaut (Figure 1), proglacial-threshold lakes whose catchments extend beneath GrIS today, show that this sector of the GrIS margin was behind its present position from at least ~5.8 to 2.3 ka (Briner et al., 2010). Following this minimum, ice advanced during the late Holocene, culminating in the deposition of the historical moraine in ~1850 CE (Weidick & Bennike, 2007). Since 1850 CE, ice-margin retreat has revealed a landscape that holds information about subglacial erosion during the most recent (historical) period of ice cover. Young et al. (2016) compared the ^{10}Be concentration in surficial bedrock samples immediately inboard (east) of the historical moraine to the ^{10}Be concentration of bedrock samples outboard of the moraine to derive a basin-wide average erosion rate of 0.75 ± 0.35 mm yr^{-1} for the period of historical ice cover. Here, we expand upon the dataset of Young et al. (2016) to capture subglacial erosion rates near the modern terminus of Jakobshavn Isbræ.

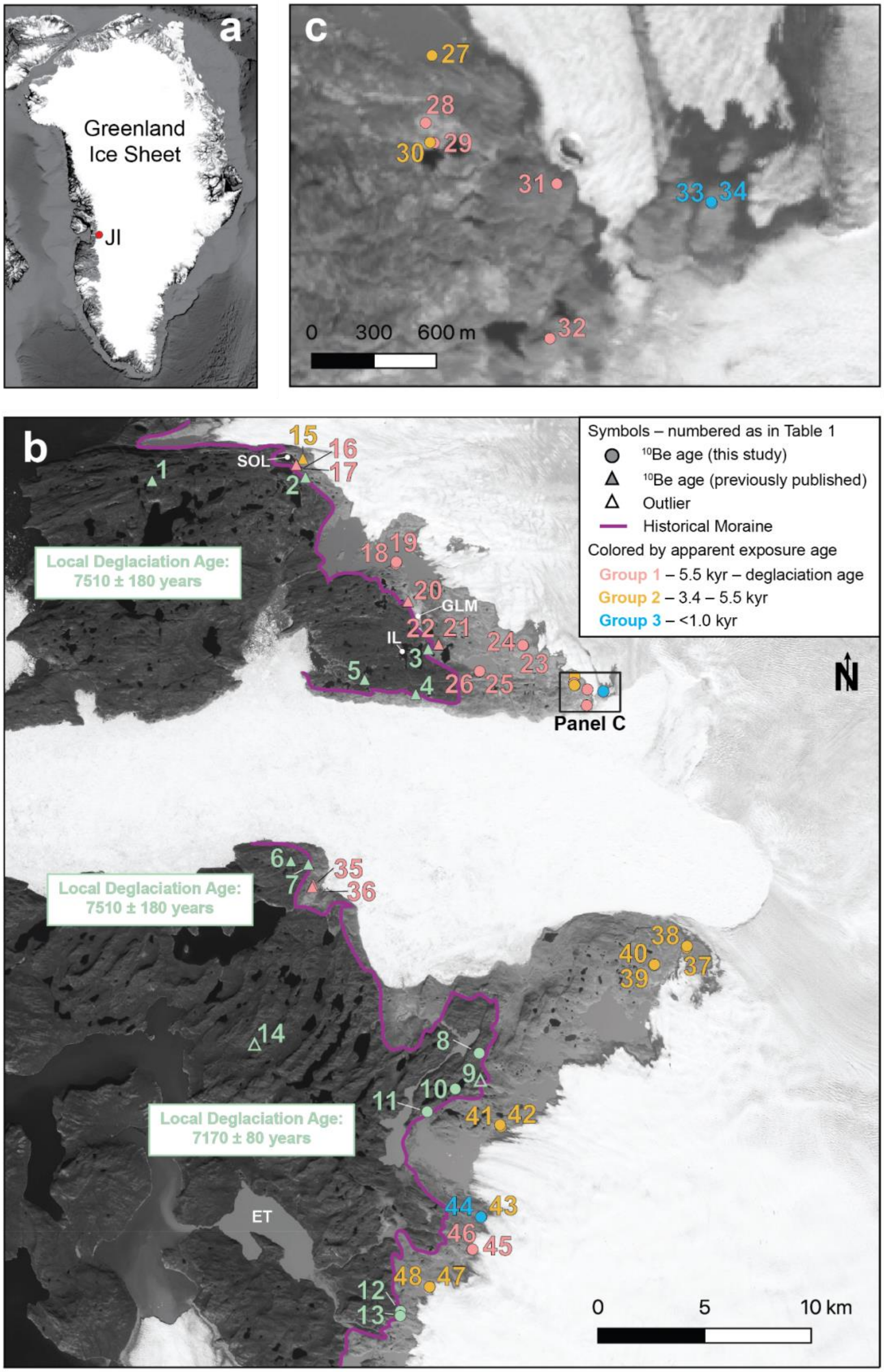
a
Greenland
Ice Sheet
JI
c
27
28
30
29
31
33
34
32
0 300 600 m
b
Symbols – numbered as in Table 1
10Be age (this study)
10Be age (previously published)
Outlier
Historical Moraine
Colored by apparent exposure age
Group 1 – 5.5 kyr – deglaciation age
Group 2 – 3.4 – 5.5 kyr
Group 3 – <1.0 kyr
SOL
GLM
IL
ET
Panel C
Local Deglaciation Age: 7510 ± 180 years
Local Deglaciation Age: 7510 ± 180 years
Local Deglaciation Age: 7170 ± 80 years
N
0 5 10 km

Figure 1. Map of the study area within the Jakobshavn Isbrae forefield. **a)** The location of Jakobshavn Isbræ (JI) in Greenland. **b)** Sample locations colored by apparent exposure age. The historical moraine and trimline is outlined in purple. Numbers correspond to sample locations in Table 1. Location information, apparent exposure ages, erosional depths and abrasion rates are also listed in Table 1. South Oval Lake (SOL), Glacial Lake Morten (GLM), Iceboom Lake (IL), and Eqaluit Taserssaut (ET) are proglacial-threshold lakes referenced in the text (Briner et al., 2011; Briner et al., 2010). **c)** Detailed view, bedrock coring site is location #29.

3 Methods

3.1 Field Methods

In August 2018, we sampled bedrock surfaces located between the historical moraine and the modern ice margin north and south of Jakobshavn Isfjord (Figure 1). Sampling locations in Young et al. (2016) were inboard of, but close to, the historical moraine. Here, we aimed to provide a complementary sample set by focusing on bedrock surfaces directly adjacent to the modern ice margin; however, one pair of samples (18JAK-37 and 18JAK-38) is located between the historical moraine and the ice margin, providing landscape coverage between previous sample locations and our 2018 sampling locations. We targeted bedrock surfaces atop whalebacks with visible evidence of glacial abrasion, such as glacial polish and striations, and avoided sediment-covered sites, locations shielded by erratic boulders, and places where quarrying appeared to be the dominant form of subglacial erosion (Figure 2). At each site, we recorded the location and elevation using handheld GPS, measured topographic shielding, and collected the upper 1–3 cm of the bedrock surface using Hilti brand AG500-A18 angle grinder-circular saw with diamond bit blades, and hammer and chisel. In addition to the surface samples, we extracted a 41-mm diameter bedrock core to 4.04-m depth using a Shaw Portable Backpack Drill.

Figure 2. Photographs of typical bedrock sampling locations in the Jakobshavn Isbræ forefield. We targeted sampling locations exhibiting evidence of abrasion (e.g., striations, glacial polish) and avoided those with evidence of plucking. **Top row:** sample locations north of Jakobshavn Isbræ. 18-JAK-CR1 is the bedrock core location. **Bottom row:** sample locations south of Jakobshavn Isbræ, where the landscape is considerably more debris-laden than the north.

3.2 Laboratory Methods

We processed samples at the Lamont-Doherty Earth Observatory cosmogenic dating laboratory following established quartz isolation and beryllium extraction procedures (e.g., Schaefer et al., 2009; https://www.ldeo.columbia.edu/cosmo/methods). $^{10}Be/^{9}Be$ ratios were measured at the Center for Accelerator Mass Spectrometry at Lawrence Livermore National Laboratory (LLNL-CAMS) relative to the 07KNSTD standard with a $^{10}Be/^{9}Be$ ratio of 2.85 x 10^{-}

^{12} (Nishiizumi et al., 2007). Surface sample ^{10}Be concentrations ranged from 3250 ± 230 to 47070 ± 1140 atoms g^{-1}, with analytical uncertainty from 1.8% to 4.9% (mean = 2.5% ± 0.8%; Table S1). Blank corrections for surface samples, calculated by subtracting the average number of ^{10}Be atoms from blanks processed with each sample batch, ranged from 0.5% to 20%, with the majority of corrections being <3.5% (Table S2). Reported uncertainties in ^{10}Be concentrations include analytical and blank errors propagated in quadrature, and uncertainties related to the ^{9}Be carrier concentration (1.5%), which are treated as systematic errors.

3.3 ^{10}Be Apparent Exposure Age Calculations

^{10}Be apparent exposure ages are calculated in MATLAB using code from Version 3 of the online exposure age calculator described by Balco et al. (2008), updated to include a computationally efficient approximation of muon production rates near the earth surface (Balco, 2017). For all exposure age calculations, we employ the regionally calibrated Baffin Bay ^{10}Be production rate (Young et al., 2013a) and the time-dependent “Lm” production rate scaling method of Lal (1991)/Stone (2000). Here, “apparent” exposure ages refer to the calculated age of the bedrock sample given the measured cosmogenic ^{10}Be inventory, assuming that the bedrock has experienced only one period of exposure with no erosion or burial during that time.

3.4 Quantifying subglacial erosion using cosmogenic ^{10}Be

Cosmogenic ^{10}Be accumulates in quartz when rock is exposed to the secondary cosmic ray flux (i.e., ice free). The ^{10}Be concentration at the bedrock surface and the rate at which it decreases with depth holds information about exposure history and subglacial erosion, which we quantify using modeled and measured ^{10}Be depth profiles (e.g., Schaefer et al., 2016; Young et al., 2016). At Earth’s surface, spallation reactions comprise the majority of production, but these high-energy neutron reactions decrease rapidly with depth [attenuation length (Λ) = 160 g cm^{-2}].

Muon interactions contribute only ~1–2% of the ^{10}Be production at the rock surface, but dominate production below ~650 g cm^{-2} (~2.5 m in rock), meaning that the percentage of muon production relative to spallation increases with depth. Muon interactions take place at all depths in rock, and produce ^{10}Be via two pathways: negative muon capture and fast muon interactions. Fast muons with higher energies remain in motion to farther depth in rock, thus the attenuation length (and proportion of production relative to negative muon capture) of fast muon ^{10}Be production increases with depth. As a result, the variation of ^{10}Be with depth is approximately exponential, taking the shape of the ^{10}Be production profile shown in Figure 3 (Balco, 2017). Here, we leverage the near-exponential and predictable shape of ^{10}Be production with depth to quantify subglacial erosion. Assuming that bedrock started with a negligible amount of ^{10}Be, the change in ^{10}Be concentration with depth in rock mirrors that of the ^{10}Be production profile at the end of an exposure period. During subsequent ice cover, subglacial erosion removes bedrock to a depth determined by the erosion rate and the duration of ice cover beginning with the upper surfaces of the rock where the majority of ^{10}Be production takes place, truncating the ^{10}Be depth profile to the erosional depth. Using this concept, we compare measured ^{10}Be concentrations to modeled ^{10}Be depth profiles to recover erosional depth at our surface sample and bedrock core locations.

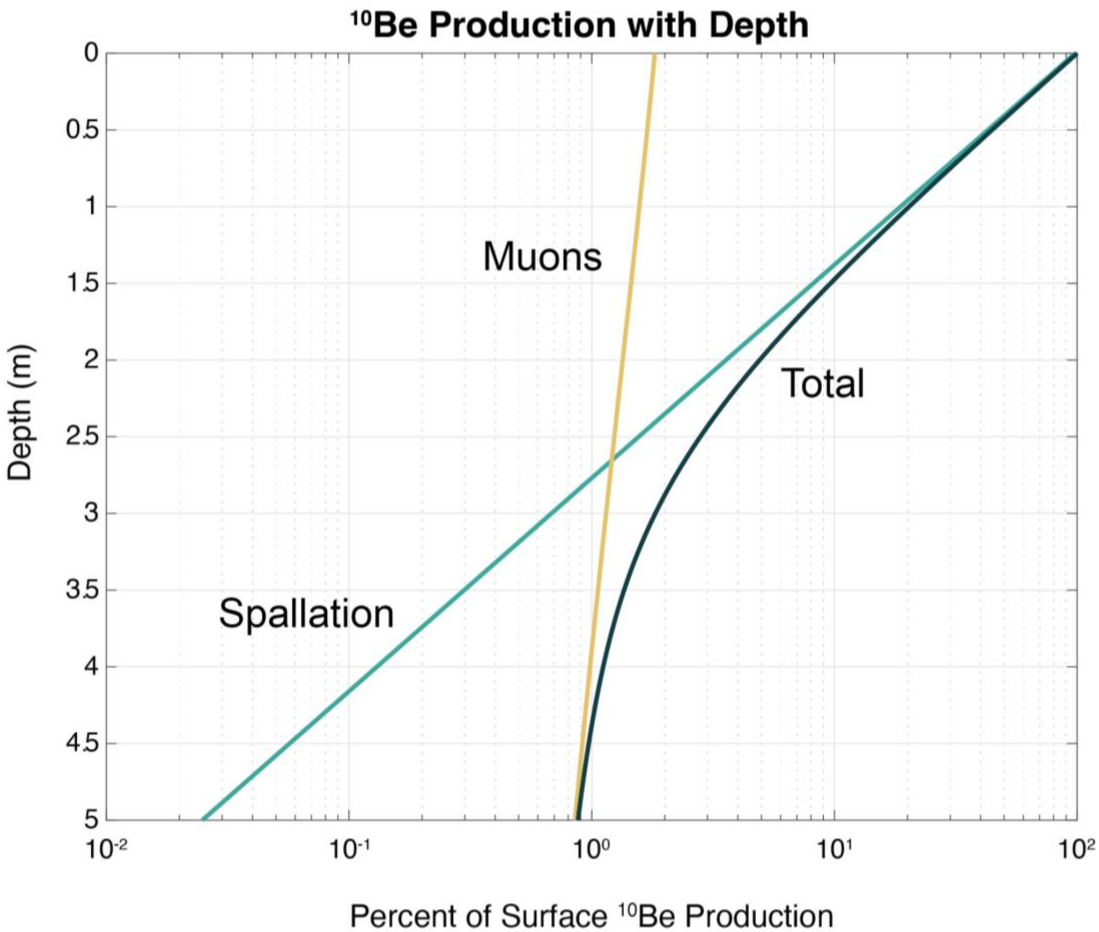

Figure 3. ^{10}Be production profile shown as percent of surface production at sea-level high latitude. Although the production rate varies with geomagnetic latitude and elevation, the relative proportion of production by muons and spallation is similar at Jakobshavn Isbræ, with ~1% production by muons at the surface. Note that by ~2.5 m depth, muon production exceeds spallation production.

The ^{10}Be concentration in bedrock fronting Jakobshavn Isbræ holds information about the duration of Holocene exposure and any subglacial erosion that took place during historical cover. Because the ice-margin history at Jakobshavn Isbræ is well constrained by basal radiocarbon ages in proglacial-threshold lakes and ^{10}Be ages outboard of the historical moraine, we are able to use ^{10}Be concentrations inboard of the historical moraine to derive subglacial erosion rates for the most recent period of ice cover. Inboard of the historical moraine, the maximum exposure age a bedrock sample can have is the local deglaciation age minus the duration of historical cover (Figure 4). We compare the ^{10}Be exposure ages from bedrock samples inboard of the historical limit to this maximum allowable exposure age; a younger-than-expected ^{10}Be age indicates that a detectable amount of subglacial erosion took place during historical cover (Young et al., 2016; Figure 4).

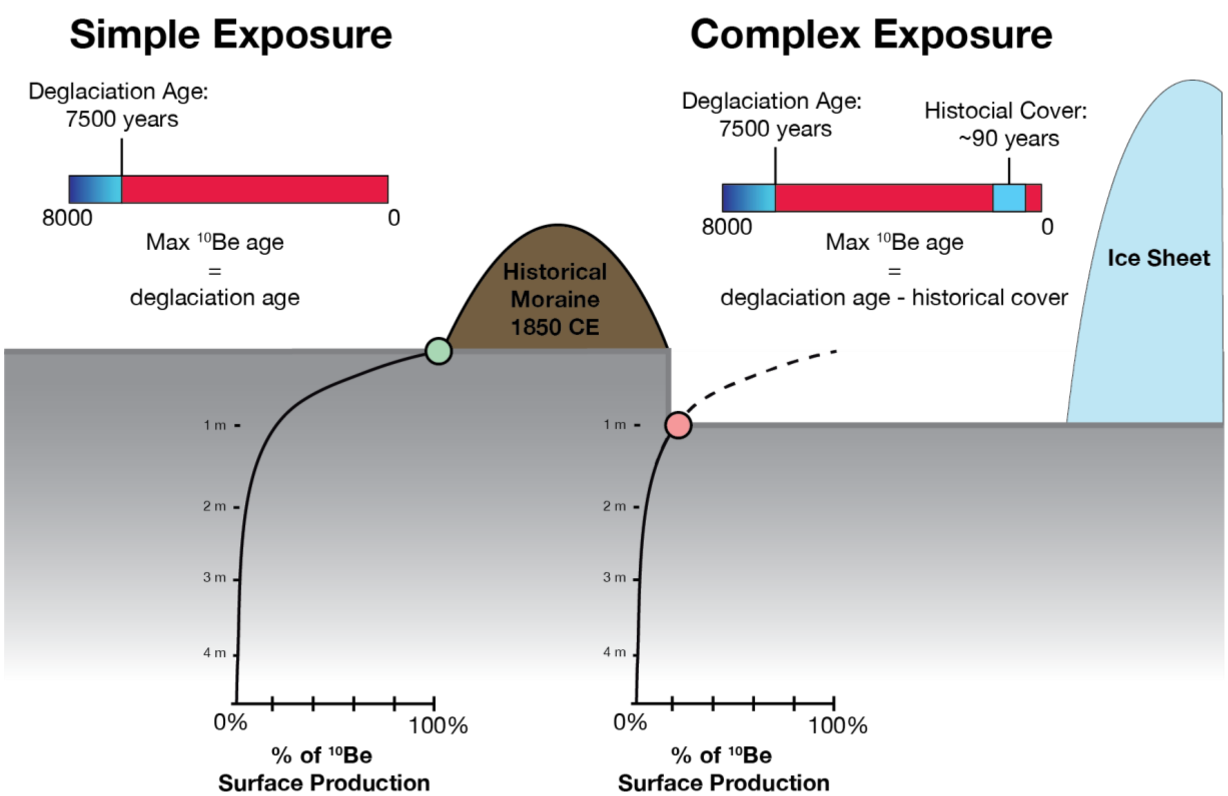

Figure 4. Schematic of the Jakobshavn Isbrae forefield describing how erosion rates are derived from the measured ^{10}Be concentrations. The bedrock outboard (left) of the historical moraine experienced only one continuous period of exposure during the Holocene, as shown in the timeline, so a surface sample collected at the light green circle would have an apparent exposure age that reflects the true deglaciation age of the site. The bedrock inboard [right; sample location similar to that of Young et al. (2016)] of the moraine, shown in pink, has a complex exposure history, including the ~90 years of ice cover at the end of the Holocene. During this most recent period of ice cover, any subglacial erosion would remove the upper portion of the ^{10}Be depth profile in the bedrock, accumulated from previous exposure, so the measured ^{10}Be concentration would be lower than the true exposure age. For the sake of illustration, a surface sample collected at the pink circle experienced 1-m of subglacial erosion during historical cover, and therefore its ^{10}Be concentration would be 20% of the expected concentration.

We determine the depth of subglacial erosion during historical cover by locating the measured ^{10}Be concentration along modeled ^{10}Be depth profiles specific to each sample location. Depth profiles are derived by projecting the spallogenic component of the surface ^{10}Be concentration commensurate with the maximum possible exposure age to an arbitrary depth using an attenuation length of 160 g cm^{-2}. The muonic component of the ^{10}Be depth profile is quantified using MATLAB code from Balco et al. (2008) [updated in Balco (2017)], which implements downward propagation of the muon energy spectrum after Heisinger et al. (2002 a, b). To find the depth of subglacial erosion during historical cover, we locate the depth (in g cm^{-2}) at which the measured ^{10}Be concentration matches that of the modeled profile. These are cast as erosional depths for different materials based on their density, such as depth in rock (2.65 g cm^{-3}). Finally, we determine uncertainty in the erosional depth from the uncertainty in deglaciation age and duration of historical cover propagated in quadrature.

In addition to quantifying subglacial erosion from surficial bedrock samples, we compare measured ^{10}Be concentrations in a 4-m long bedrock core to modeled depth profiles derived using the known exposure history at the core location. To simulate subglacial erosion during the most recent period of ice cover, we assume that the modern bedrock surface was covered by additional mass (in this case, rock) when the core site was first exposed during the Holocene (e.g., Schaefer et al., 2016). We then find the best-fitting ^{10}Be depth profile by adjusting how far below the modern surface the bedrock was when the measured ^{10}Be accumulated. The depth of this adjustment is equivalent to the erosional depth during historical cover at the core site.

4 Results

4.1 Apparent exposure ages in surficial bedrock samples

Five new ^{10}Be measurements on bedrock just outboard of the historical moraine refine the timing of local deglaciation south of Jakobshavn Isfjord to 7170 ± 80 years (mean ± SD), which is slightly younger than the deglaciation age for the northern part of the study area of 7510 ± 180 years [n=7; statistically identical to deglaciation age of Young et al. (2016), but re-calculated using v3 of the online calculator described in Section 3.3] (Figure 1; Table 1). Twenty-six new ^{10}Be measurements from bedrock within the trimline are located throughout the study area and yield apparent exposure ages that range from 730 ± 50 to 7600 ± 170 years (Figure 1; Table 1). Three distinct age groupings emerge from these data: 13 ^{10}Be ages that are between 5700 years and the local deglaciation age (Group 1), eight of which overlap the local deglaciation age within uncertainty; 11 ^{10}Be ages that date between ~3400 and ~5000 years (Group 2), and three ^{10}Be ages are <1000 years (Group 3). Of the eight ^{10}Be ages from bedrock inboard of the historical limit published by Young et al. (2016), which are considered alongside our new dataset, seven fall in Group 1 and one falls in Group 2.

4.2 Bedrock core beryllium-10 concentrations

Seventeen ^{10}Be measurements in bedrock core 18JAK-CR1 afford ^{10}Be concentrations that range from 26,420 ± 630 atoms g^{-1} in the uppermost sample (0–8 cm) to 620 ± 60 atoms g^{-1} in the lowest sample (374.1 – 404.8 cm) (Table 2). The surface sample 18JAK-CR1-SURFACE, which we collected from bedrock immediately bordering the borehole (sample thickness = 1.29 cm), has a ^{10}Be concentration of 33420 ± 8340 atoms g^{-1}, which equates to an apparent exposure age of 7140 ± 180 years. Both analytical uncertainty and blank corrections in the bedrock core generally increase downcore (owing to rapidly decreasing ^{10}Be concentrations), ranging from 2.2% and 7.2% and 1.6% to 16.6%, respectively (Table S2).

Table 1 - Exposure ages and erosion rates from surficial bedrock samples at Jakobshavn Isbræ.

Number in Figure 1	Sample ID	Location	Historical Cover (years)	Age (Lm years ± SD)	Rock Erosion Depth (cm)	Abrasion rate (mm yr^{-1})	Sediment Erosion Depth (cm)[1]	Sediment Erosion Depth + Bedrock Erosion (cm)[2]	Rock Erosion Depth + Bedrock Erosion (cm)[3]	Reference
Outboard of Historical Moraine										
1	JAKN08-56	North	-	7480 ± 180	-	-	-	-	-	Young et al., 2011
2	JAKN08-44	North	-	7350 ± 280	-	-	-	-	-	Young et al., 2011
3	JAKN08-28	North	-	7410 ± 360	-	-	-	-	-	Young et al., 2011
4	JAKN08-39	North	-	7430 ± 240	-	-	-	-	-	Young et al., 2011
5	JAKN08-40	North	-	7890 ± 200	-	-	-	-	-	Young et al., 2011
6	JAKS08-33	South (Fjord-adjacent)	-	7550 ± 320	-	-	-	-	-	Young et al., 2011
7	JAKS08-34	South (Fjord-adjacent)	-	7440 ± 190	-	-	-	-	-	Young et al., 2011
				***Local deglaciation age:* 7510 ± 180 years**						
8	JAKS08-12	South	-	7090 ± 150	-	-	-	-	-	This study
9	JAKS08-08	South	-	6490 ± 160	-	-	-	-	-	Young and Briner, 2015
10	JAKS08-05	South	-	7140 ± 190	-	-	-	-	-	This study
11	JAKS08-04	South	-	7120 ± 140	-	-	-	-	-	This study
12	09GRO-19	South	-	7220 ± 150	-	-	-	-	-	This study
13	09GRO-20	South	-	7280 ± 140	-	-	-	-	-	This study
14	JAKS08-24	South	-	7610 ± 340	-	-	-	-	-	Young et al., 2011
				***Local deglaciation age:* 7170 ± 80 years**						
Inboard of Historical Moraine										
Group 1 - Apparent age 5700 years to local deglaciation age										
18	18JAK-29	North	200 ± 1	7490 ± 190	<0.81	<0.04	-	-	-	This study
19	18JAK-30	North	200 ± 1	7390 ± 140	<1.00	<0.05	-	-	-	This study

Table 1 - continued.

Number in Figure 1	Sample ID	Location	Historical Cover (years)	Age (Lm years ± SD)	Rock Erosion Depth (cm)	Abrasion rate (mm yr^{-1})	Sediment Erosion Depth (cm)[1]	Sediment Erosion Depth + Bedrock Erosion (cm)[2]	Rock Erosion Depth + Bedrock Erosion (cm)[3]	Reference
Group 1 cont'd - Apparent age 5700 years to local deglaciation age										
24	18JAK-28	North	202 ± 2	7490 ± 200	<0.84	<0.04	-	-	-	This study
25	18JAK-37	North	87 ± 27	7600 ± 170	<0.70	<0.08	-	-	-	This study
26	18JAK-38	North	87 ± 27	7500 ± 130	<0.95	<0.11	-	-	-	This study
31	18JAK-39	North	219 ± 2	7210 ± 300	0.71 ± 2.38	0.03 ± 0.11	-	-	-	This study
45	18JAK-13	South	222 ± 1	7380 ± 140	0	0	-	-	-	This study
46	18JAK-14	South	222 ± 1	7470 ± 140	0	0	-	-	-	This study
16	JAKN08-50	North	87 ± 27	7020 ± 140	3.42 ± 2.71	0.39 ± 0.31	-	-	-	Young et al., 2016
17	JAKN08-49	North	87 ± 27	7040 ± 140	3.20 ± 2.69	0.37 ± 0.31	-	-	-	Young et al., 2016
20	JAKN08-29	North	87 ± 27	6780 ± 140	5.49 ± 2.74	0.63 ± 0.31	-	-	-	Young et al., 2016
21	JAKN08-41	North	87 ± 27	6560 ± 110	7.55 ± 2.51	0.87 ± 0.29	-	-	-	Young et al., 2016
22	JAKN08-42	North	87 ± 27	6740 ± 130	5.91 ± 2.69	0.68 ± 0.31	-	-	-	Young et al., 2016
23	18JAK-27	North	202 ± 2	7030 ± 140	2.33 ± 2.53	0.12 ± 0.13	-	-	-	This study
28	18JAK-CR2-SURFACE	North	213 ± 1	6910 ± 130	3.37 ± 2.67	0.16 ± 0.13	-	-	-	This study
29	18JAK-CR1-SURFACE	North	213 ± 1	7140 ± 180	1.30 ± 2.17	0.06 ± 0.10	-	-	-	This study
32	18JAK-40	North	213 ± 1	6900 ± 150	3.38 ± 2.85	0.16 ± 0.13	-	-	-	This study
35	JAKS08-36	South (Fjord-adjacent)	87 ± 27	6570 ± 140	7.45 ± 2.83	0.86 ± 0.32	-	-	-	Young et al., 2016
36	JAKS08-37	South (Fjord-adjacent)	87 ± 27	6400 ± 130	9.10 ± 2.77	1.05 ± 0.32	-	-	-	Young et al., 2016
47	18JAK-11	South	217 ± 1	5780 ± 130	11.31 ± 2.08	0.52 ± 0.10	-	-	-	This study
				Group Average:	3.44 ± 3.30	0.31 ± 0.34	-	-	-	

Table 1 - continued.

Number in Figure 1	Sample ID	Location	Historical Cover (years)	Age (Lm years ± SD)	Rock Erosion Depth (cm)	Abrasion rate (mm yr^{-1})	Sediment Erosion Depth (cm)[1]	Sediment Erosion Depth + Bedrock Erosion (cm)[2]	Rock Erosion Depth + Bedrock Erosion (cm)[3]	Reference
Group 2 - Apparent age 3400 to 5500 years										
15	JAKN08-51	North	87 ± 27	4910 ± 100	25.27 ± 2.78	2.90 ± 0.32	33.48 ± 3.68	29.90	22.57	Young et al., 2016
27	18JAK-26	North	220 ± 1	5010 ± 110	22.96 ± 2.88	1.04 ± 0.13	30.42 ± 3.82	21.37	16.13	This study
30	18JAK-25	North	213 ± 0	3770 ± 100	40.58 ± 3.15	1.91 ± 0.15	53.77 ± 4.17	45.01	33.97	This study
37	18JAK-35	South	216 ± 0	4460 ± 120	27.24 ± 2.3	1.26 ± 0.11	36.09 ± 3.05	27.21	20.53	This study
38	18JAK-36	South	216 ± 0	3430 ± 70	43.45 ± 2.04	2.01 ± 0.09	57.57 ± 2.70	48.69	36.74	This study
39	18JAK-33	South	185 ± 10	3720 ± 80	38.69 ± 2.07	2.09 ± 0.11	51.26 ± 2.74	43.66	32.95	This study
40	18JAK-34	South	185 ± 10	4750 ± 100	23.62 ± 2.00	1.28 ± 0.11	31.30 ± 2.65	23.69	17.88	This study
41	18JAK-17	South	222 ± 1	3680 ± 110	38.99 ± 2.58	1.76 ± 0.12	51.66 ± 3.41	42.53	32.10	This study
42	18JAK-18	South	222 ± 1	4690 ± 120	24.14 ± 2.27	1.09 ± 0.10	31.99 ± 3.00	22.85	17.25	This study
43	18JAK-15	South	222 ± 1	4190 ± 90	30.99 ± 2.05	1.40 ± 0.09	41.06 ± 2.72	31.93	24.10	This study
48	18JAK-12	South	217 ± 1	4450 ± 80	27.29 ± 1.85	1.26 ± 0.09	36.16 ± 2.45	27.23	20.55	This study
				Group Average:	31.0 ± 7.7	1.63 ± 0.56	41.34 ± 10.23	33.10	24.98	This study
Group 3 - Apparent age <1000 years										
33	18JAK-23	North	216 ± 0	730 ± 50	146.97 ± 6.32	6.80 ± 0.29	194.74 ± 8.37	185.85	140.26	This study
34	18JAK-24	North	216 ± 0	869 ± 44	134.87 ± 5.1	6.24 ± 0.24	178.70 ± 6.76	169.82	128.16	This study
44	18JAK-16	South	222 ± 1	920 ± 40	126.51 ± 3.61	5.70 ± 0.16	167.63 ± 4.78	158.49	119.62	This study
				Group Average:	136.0 ± 10.4	6.24 ± 0.56	180.35 ± 13.63	171.39	129.35	

[1]Only calculated for samples interpreted to have possible sediment cover. Assume till density of 2.0 g cm^{-3}

[2]Sediment cover atop site during Holocene, assuming that bedrock was then abraded at the site-wide average rate of 0.31 mm yr^{-1} during historical cover.

[3]Same assumptions as [2], but if the site were covered by a boulder or boulder-rich till prior to historical cover.

Table 2 - ^{10}Be concentrations in bedrock core 18JAK-CR1

Sample ID	Top Depth (cm)	Bottom Depth (cm)	Quartz Weight (g)	Carrier Added (g)	^{10}Be/^{9}Be Ratio (x 10^{-14})	^{10}Be/^{9}Be Ratio 1σ Uncertainty (x 10^{-15})	Blank-corrected ^{10}Be (atoms/g)	Blank-corrected ^{10}Be uncertainty (atoms/g)	Blank[1]
18JAK-CR1-SURFACE	0	1.29	30.2287	0.1798	8.34	2.03	33420	834	B2
18JAK-CR1-1	0	8	17.3245	0.1807	4.32	1.00	30498	721	B11, B12
18JAK-CR1-2	10	18	21.3586	0.1825	4.58	1.06	26423	632	B7, B8, B9, B10
18JAK-CR1-3	20	28	23.0615	0.1826	4.19	0.92	22340	509	B7, B8, B9, B10
18JAK-CR1-4	30	38	20.0823	0.1823	3.07	0.73	18652	468	B7, B8, B9, B10
18JAK-CR1-5	40	50	25.7314	0.1820	3.39	0.77	16081	387	B7, B8, B9, B10
18JAK-CR1-6	50	61	37.9532	0.1825	4.14	1.66	13432	551	B7, B8, B9, B10
18JAK-CR1-7	61	72.3	27.6631	0.1824	2.6	0.70	11503	323	B11, B12
18JAK-CR1-8	78.7	91.1	36.3062	0.1825	2.46	0.70	8228	249	B7, B8, B9, B10
18JAK-CR1-9	98.8	115	50.5713	0.1832	2.47	0.73	5943	187	B7, B8, B9, B10
18JAK-CR1-10	121.1	136.4	48.7735	0.1815	1.72	0.60	4239	157	B11, B12
18JAK-CR1-11	150	167	59.9452	0.1817	1.50	0.66	3000	141	B11, B12
18JAK-CR1-12	198.2	228.2	69.0665	0.1829	0.99	0.47	1657	93	B7, B8, B9, B10
18JAK-CR1-12B	246.9	274.8	74.235	0.1815	0.80	0.38	1107	70	B13
18JAK-CR1-12C	274.8	298.2	71.9527	0.181	0.71	0.33	978	64	B13
18JAK-CR1-13	298.2	328.2	88.4342	0.1823	0.78	0.48	1006	70	B11, B12
18JAK-CR1-13B	328.2	359.2	98.1764	0.1817	0.79	0.37	824	51	B13
18JAK-CR1-14	374.1	404.8	98.7781	0.1829	0.57	0.41	621	57	B7, B8, B9, B10

[1]See Table S2 for blank values.

5 Ice Margin History

To calculate erosion depths and rates, we compare measured ^{10}Be concentrations to the maximum allowable ^{10}Be concentrations as defined by the local ice-margin history. Broadly, ice retreated across the study area ~7500 years ago to a position smaller than present, and then readvanced during the late Holocene, culminating in deposition of the historical moraine in 1850 CE (Figure 1). Following the deposition of the historical moraine, the ice-margin retreated towards the present margin, and continues to retreat today. Here, we estimate the local deglaciation age for each part of our study area and determine the likely total duration of historical cover at each sample location that can be used to constrain erosion rates.

The local deglaciation age at Jakobshavn Isbræ is determined by ^{10}Be ages in bedrock just outboard of the historical moraine and, assuming continued rapid retreat of the ice margin, marks the time when ice retreated across the study area, also starting the cosmogenic clock for our sample locations inboard of the moraine (Young et al., 2016). In the southern part of our study area, five new ^{10}Be ages from bedrock outboard of the historical limit reveal that the deglaciation age south of Jakobshavn Isbræ (7170 ± 80 years) is slightly younger than the deglaciation age north of Jakobshavn Isbræ (7510 ± 180 years). Although the northern and southern deglaciation ages overlap within 2σ, several lines of evidence suggest that the younger age reflects later ice-margin retreat from the landscape fronting GrIS south of Jakobshavn Isbræ. First, basal radiocarbon ages from proglacial-threshold lakes indicate that the GrIS margin south of Jakobshavn Isbræ likely retreated during deglaciation behind its 2018 position slightly later than, and re-advanced during the Late Holocene beyond the 2018 position earlier than, the margin north of Jakobshavn Isbræ. A radiocarbon age near the base of the most recent organic unit in Loon Lake indicates that the GrIS margin did not retreat out of its catchment before

~6300 cal yr BP, suggesting delayed retreat across the southern landscape relative to north of the fjord (minimum age; Briner et al., 2010). Delayed retreat from this landscape is further corroborated by the earlier re-advance of the GrIS into the nearby Goose Lake catchment by ~2500 cal yr BP, indicating that the GrIS margin south of Jakobshavn Isbræ spent comparatively less of the Holocene behind its current position (Briner et al., 2010), which can in part be achieved by delayed initial deglaciation. Second, sample JAKS08-24 located ~12 km outboard of the historical moraine south of Jakobshavn Isbræ, at a similar westward position as the historical moraine north of Jakobshavn Isfjord, has an age of 7610 ± 340, which is commensurate with the deglaciation age of the north. Collectively, these chronological constraints suggest that (i) the younger deglaciation ages outboard of the historical moraine south of Jakobshavn Isbræ reflect the true deglaciation age of this landscape, and (ii) the bedrock positioned between the historical moraine and the GrIS margin likely experienced slightly less total surface exposure than the equivalent bedrock landscape directly adjacent to and north of Jakobshavn Isford.

Assuming the quick and continuous retreat of the ice margin (Young et al., 2011; Young et al., 2016), the local deglaciation age marks the maximum amount of ^{10}Be that any bedrock surface can have, whether it is immediately inboard of the historical moraine or adjacent to the modern ice margin. For our new ice-marginal sites, eight ^{10}Be ages from Group 1 overlap with the local deglaciation age, confirming that the local deglaciation age calculated from ^{10}Be beyond the historical moraine indeed marks the start of the cosmogenic clock for these ice-marginal locations. Furthermore, the overlap of Group 1 ages with the deglaciation age further constrains the minimum extent of inland GrIS retreat during the mid-Holocene, as the ice margin must have retreated rapidly across the landscape just now emerging in front of Jakobshavn Isbræ, withdrawing to within the 2018 margin by ~7500 years ago in the north, and ~7200 years ago in the south. Although we cannot determine with these data where the GrIS margin was positioned at its most retracted Holocene extent, the ice-marginal ages that overlap with the local deglaciation age confirm that this sector of the GrIS was inland of the 2018 CE margin during mid-Holocene warmth.

Lake sediment records and historical observations constrain when ice advanced across the landscape immediately inboard of the historical moraine during the late Holocene (Briner et al., 2011). Varved sediments indicate that Iceboom Lake, a proglacial-threshold lake whose catchment threshold is located east of the sample locations of Young et al. (2016), but west of our 2018 sample collection, became glacially fed in ~1820 CE (Briner et al., 2011) and historical observations show the GrIS at its historical maximum before 1850 CE (Weidick, 1968). Historical observations place the GrIS margin at its historical maximum until at least 1900 CE (Weidick, 1968) and aerial imagery documents the subsequent glacial retreat, showing the GrIS margin just east of the sample locations inboard of the historical limit in 1944 CE (Csatho et al., 2008). Using these constraints, Young et al. (2016) determined that the sites immediately inboard of the historical moraine became ice covered in 1835 ± 15 CE (midpoint between 1820 CE and 1850 CE) and became ice-free in 1922 ± 22 CE (midpoint between 1900 CE and 1944 CE), meaning that those sites were covered for 87 ± 27 years during the period of recent historical ice cover (Young et al., 2016; Table 1). However, our new bedrock locations are farther east (adjacent to the modern ice margin) and thus would have become ice-covered earlier as ice advanced during the late Holocene, and became ice-free more recently, than the bedrock sites of Young et al. (2016).

To estimate the timing of ice advance across our sample locations, we rely on the sediment record of Glacial Lake Morten, situated just north of Jakobshavn Isfjord (Briner et al., 2011; Figure 1). Glacial Lake Morten is a drained, formerly ice-dammed proglacial lake for which satellite imagery documents ice retreat out of the lake's catchment, and thus draining of the lake, between 1986–1991. Therefore, the 1991 ice terminus position is the approximate eastern limit of the lake catchment. Using that catchment boundary, we hypothesize that when Glacial Lake Morten became glacially fed as ice advanced toward the historical limit during the late Holocene, the GrIS ice margin position was similar to its 1991 configuration. In Landsat imagery from 1991, all of our ice-marginal sample locations were ice covered, so we estimate that the latest ice could have advanced across our sample locations during the late Holocene is coincident with the advance of ice into the Glacial Lake Morten catchment.

Layer counting of varved sediments from Glacial Lake Morten reveal that ice advanced into the basin between 1795–1800 CE, and thus the latest our ice-marginal bedrock sites may have become ice covered is ~1795 CE. Finally, our ice-marginal sites became ice-free most recently during the satellite era, so we use Landsat imagery viewed in Google Earth to determine when each site became exposed as Jakobshavn Isbræ and adjacent margins retreated in recent decades (Table 1). Using the above, we estimate the total late Holocene burial duration at our ice-marginal sites range from 185 to 222 years (Table 1). For the replicate pair 18JAK-37/18JAK-38, located about halfway between the historical moraine and the 2018 margin, we use 87 ± 27 years for the duration of historical cover as those sites were deglaciated before the first Landsat imagery in 1972 and likely have a similar burial history as the previously sampled locations adjacent to the historical moraine Young et al. (2016). In sum, the maximum duration of Holocene exposure used at each sample location to model the ^{10}Be depth profiles from which our erosion rates are derived ranges from 6950 and 7420 years (Table 1).

6 Subglacial Erosion beneath the GrIS

6.1 Centennial-scale erosion

To calculate subglacial erosion rates, we compare the measured ^{10}Be concentrations in our surficial bedrock samples to the expected ^{10}Be concentrations obtained from the maximum Holocene exposure duration under zero subaerial erosion (Section 5). A measured ^{10}Be concentration less than expected (after considering the burial durations described above) likely reflects erosion through the upper portion of the ^{10}Be production profile. A ^{10}Be concentration more than expected indicates isotopic inheritance from pre-Holocene (and likely pre-Last-Glacial-Maximum) exposure. All of our measured ^{10}Be ages at the ice-marginal sites are equal to or less than the maximum Holocene exposure duration (i.e., do not contain detectable inherited ^{10}Be), and the corresponding ^{10}Be concentrations equate to ~0–150 cm of rock removed during historical ice cover. Erosional depths for the three apparent age groupings equate to ~0–11 cm (Group 1), ~23–43 cm (Group 2), and ~125–150 cm (Group 3) (Table 1; Figure 5). Of the eight erosional depths published by Young et al. (2016), seven belong to Group 1 and one to Group 2.

The distinct groupings of erosional depths (versus a random distribution of samples) in our dataset suggest that multiple subglacial processes are represented. Because we targeted bedrock locations that exhibited evidence of subglacial abrasion (i.e., striations, polish), rather than quarrying (Figure 2), we consider our erosional depths to represent abrasion depths. While it is likely that samples in erosional Group 1 represent abrasion, no sample plots between Groups 1 and 2 on Figure 1, and the apparent abrasion rates (erosion depths corrected for the duration of historical cover) implied by the erosional depths of Groups 2 (1.63 ± 0.56 mm yr^{-1}) and 3 (6.24 ± 0.56 mm yr^{-1}) exceed most estimates of subglacial erosion (which include both abrasion and quarrying) in Greenland (Hogan et al., 2020 and references therein) and as well as many estimates from the midlatitudes and polar regions (Cook et al., 2020; Figure 5). Thus, we find it unlikely that the Group 2 and 3 ^{10}Be concentrations were solely achieved by rock abrasion. There are two alternative explanations for the lower ^{10}Be concentrations (higher apparent erosional depths) of Groups 2 and 3: i) these sites were ice-covered for more of the Holocene; and/or ii) these sites were covered by sediment following initial deglaciation ca. 7500 yrs ago, which was removed during historical cover, meaning that the ^{10}Be that accumulated during the Holocene would have done so at a significantly lower production rate.

The spatial distribution of these erosion groupings helps to elucidate which of the above explanations are most plausible. The agreement between neighboring sample pairs indicates that abrasion rates are generally consistent across several meters (Figure 1). However, there are two exceptions: pair 18JAK-CR1-SURFACE (Group 1)/18JAK-25 (Group 2) north of the fjord, and pair 18JAK-15 (Group 2)/18JAK-16 (Group 3) south of the fjord (Figure 1; Table 1). The difference in abrasion rate within these pairs is surprising because i) replicate samples were only a few meters apart, and therefore would have experienced the same ice-margin history, ii) each sample in these pairs was collected from sculpted bedrock atop whalebacks that looked like

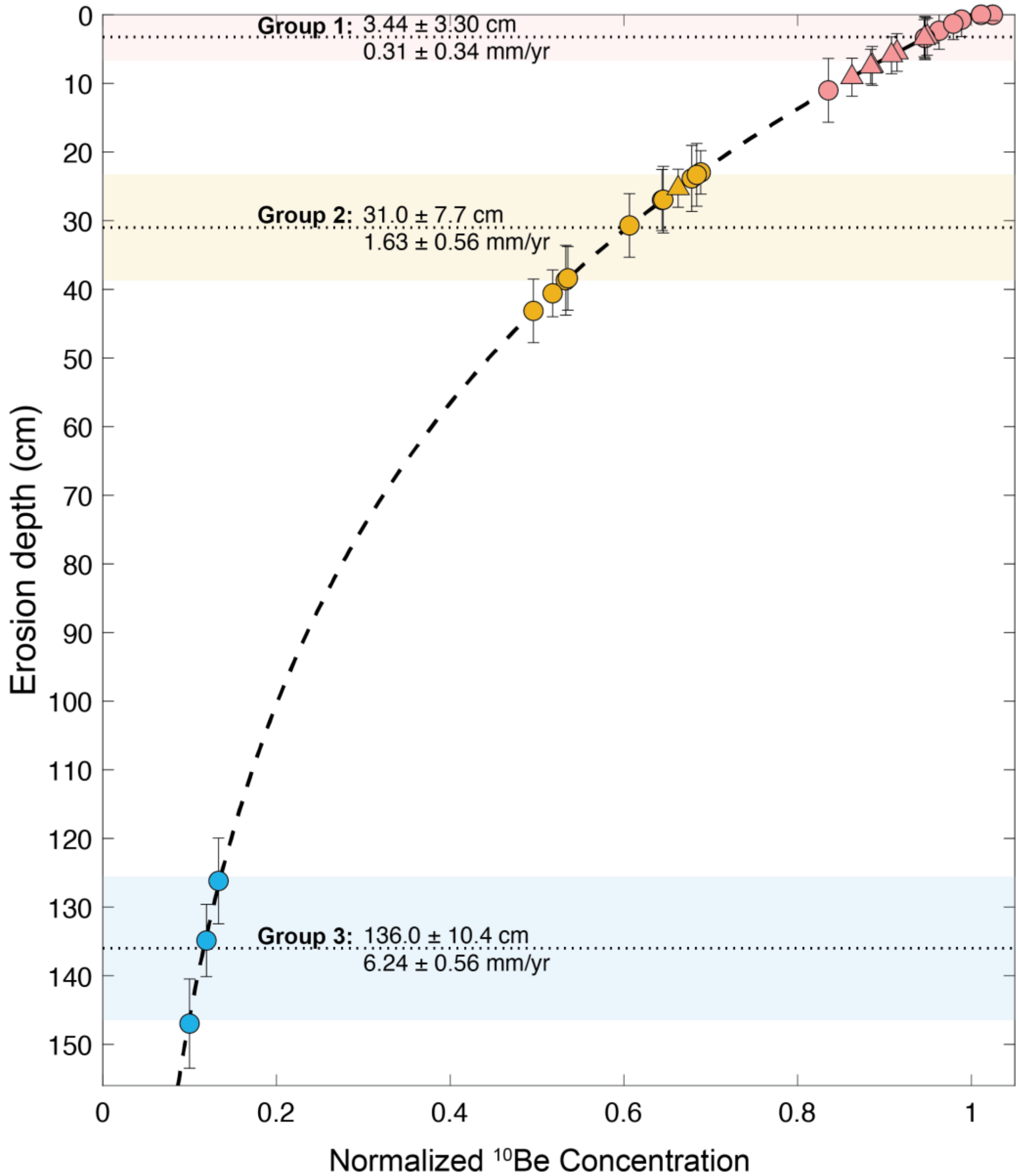

Figure 5. Calculated erosional depths and abrasion rates from ^{10}Be measurements in surficial bedrock samples inboard of the historical moraine near Jakobshavn Isbræ. The dashed line is the ^{10}Be production profile, normalized to surface production. Note that this line is not fit to the calculated erosion depths, rather this production profile is used to determine erosional depths so all data will fall on this line. Symbols are colored according to apparent exposure age as in Figure 1, circles represent data from this study and triangles show results from Young et al. (2016). The mean erosional depth for each group is plotted as a horizontal dashed black line, and the average erosional depth and abrasion rate (mean ± SD) are plotted above and below the line, respectively. Abrasion rates were determined using site-specific durations of historical cover, ranging from 87–222 years.

abraded, rather than quarried, surfaces, and iii) all samples were of the same lithology and not covered by sediment at the time of sample collection. The factors thought to control subglacial erosion (basal sliding velocity, climate, and the amount of meltwater at the bed) vary on greater-than-meter scale (Alley et al., 2019; Koppes et al., 2015), so it is unlikely that abrasion rates would vary significantly across sample replicates. In addition, the distribution of samples from Group 2 throughout the study area (Figure 1), and, in several cases, their position near samples that overlap with the deglaciation age, suggests that shorter Holocene exposure does not explain the relatively low ^{10}Be concentrations in Group 2. Rather, we observe that most (although not all) Group 2 samples are located south of Jakobshavn Isfjord (Figure 1; Table 1), where the landscape is substantially more debris-laden than the north side (Figure 2). Therefore, we suggest that during initial deglaciation, the retreating GrIS left the Group 2 sample locations covered in sediment (till), which resulted in lower ^{10}Be production at the bedrock surface during the middle Holocene, before the till was subsequently stripped from the landscape during the period of historical ice cover.

Sediment cover during the Holocene may also explain the substantially higher apparent erosion depths (low ^{10}Be concentrations) of Group 3. Two of the three Group 3 samples (8JAK-23 and 18JAK-24), however, are located in the easternmost part of the study area on a nunatak that was just emerging from the ice at the time of collection (2018); Landsat imagery from 2012, viewed in Google Earth, shows the nunatak completely ice covered. It is possible that the retreating ice margin may just now be revealing a landscape that was ice-covered for most of the Holocene, which could explain the extremely low ^{10}Be concentrations in samples 18JAK-23 and 18JAK-24. If so, the GrIS margin likely stabilized near its current position during mid-Holocene warmth and the magnitude of ongoing retreat is nearly unprecedented during the Holocene. Yet, similar work in the Kangiata Nunaata Sermia region in southwest Greenland suggests that the ice margin has yet to retreat behind its minimum Holocene extent (Young et al., 2021). In sum, the low ^{10}Be concentrations of 18JAK-23 and 18JAK-24 could tentatively represent the ice margin revealing unprecedented terrain, or could indicate significant sediment cover, but we cannot distinguish between the two scenarios with our current dataset.

By recasting the erosional depths as sediment depths using a material density appropriate for till (2.0 g cm^{-3}), sites from Groups 2 and 3 could have been covered by 30–58 cm and 168–195 cm, respectively, of sediment that shielded bedrock between the timing of deglaciation and late Holocene re-advance. While rock cover and sediment cover are two endmember scenarios, we also present a mixed model whereby sediment was removed and then bedrock abraded at the site-wide average rate of 0.31 mm yr^{-1} (see below). Using this model, 20–50 cm and 160–190 cm of sediment covered these sites for Groups 2 and 3, respectively (Table 1). Although we cannot distinguish between rock cover, sediment cover, and ice-margin history with our current ^{10}Be dataset, the spatial distribution of samples from Groups 2 and 3 point to a role for sediment cover in yielding such high erosional depths.

We suspect that Group 2 and 3 samples experienced sediment cover, longer Holocene ice cover, or both, and thus we exclude these samples when calculating an average abrasion rate for the study area. To derive abrasion rates from the Group 1 erosional depths, we correct for the duration of historical cover, which yields abrasion rates of <0.04–1.05 mm yr^{-1} (Table 1). We sampled only bedrock with evidence of recent subglacial abrasion (striations, polish, within trimline), so we know that some amount of non-zero subglacial erosion (even if small) occurred during historical cover at these sites. Since eight of the erosional depths in Group 1 overlap with zero cm, these samples are at the detection limit for our method of determining erosional depths. Therefore, we use the upper limit of the abrasion rate range for the samples overlapping 0 cm erosion when determining a site-wide average, but note that using a value of zero for all of these samples only lowers the average abrasion rate by 0.03 mm yr^{-1}. Combined, the average historical abrasion rate derived from bedrock in the Jakobshavn Isbræ forefield is 0.31 ± 0.34 mm yr^{-1} (Table 1). Integrated basin-wide erosion rates are often derived using sediment volume measurements from proglacial rivers or marine basins (e.g., Bierman & Steig, 1996; Cowton et al., 2012; Koppes et al., 2015). Unlike our point measurements, these records smooth variability throughout the glacier catchment and, crucially, include the effects of quarrying, which could account for ~30–60% of total subglacial erosion (Hallet, 1996; Riihimaki, 2005). To best compare our results to these studies, we scale our abrasion rates to estimate a total basin-wide erosion rate beneath Jakobshavn Isbræ of 0.4–0.8 mm yr^{-1} during the period of historical ice cover.

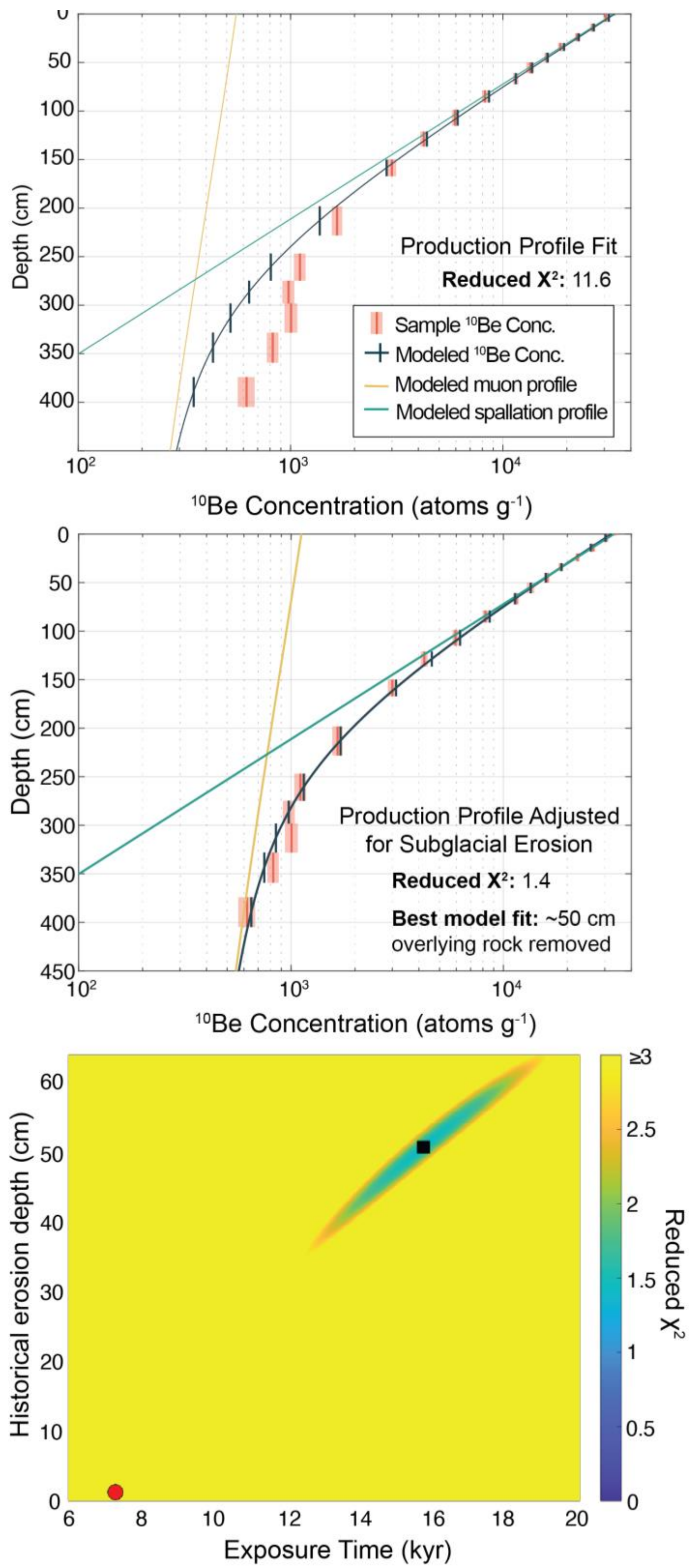

Production Profile Fit
Reduced X²: 11.6
Sample ¹⁰Be Conc.
Modeled ¹⁰Be Conc.
Modeled muon profile
Modeled spallation profile
Depth (cm)
¹⁰Be Concentration (atoms g⁻¹)
Production Profile Adjusted for Subglacial Erosion
Reduced X²: 1.4
Best model fit: ~50 cm overlying rock removed
Depth (cm)
¹⁰Be Concentration (atoms g⁻¹)
Historical erosion depth (cm)
Exposure Time (kyr)
Reduced X²

Figure 6. ^{10}Be production rate curves fit to measured ^{10}Be concentrations in 4-m-long bedrock core 18JAK-CR1. **Top:** Best-fitting ^{10}Be production profile with depth. Here, the curve is fit by multiplying the ^{10}Be production rate curve by a scalar that is roughly equivalent to the exposure age. Widths of red boxes show 1σ measurements uncertainty. Measured ^{10}Be concentrations below ~2 m depth are consistently higher than those predicted from the ^{10}Be production with depth, giving a poor fit to the data overall. **Middle:** Best-fitting ^{10}Be depth profile adjusted for mass cover prior to the historical period (i.e., adjusted for subglacial erosion during historical ice cover). Predicted ^{10}Be concentrations are consistent with measured concentrations throughout the core. **Bottom:** Historical erosion rate and exposure age used to find the best-fitting curve in the middle panel. Best-fitting scenario shown as a black square. Red circle denotes the erosion rate and exposure age calculated from the ^{10}Be concentration of the surface sample 18JAK-CR1-SURFACE, taken from the bedrock surface immediately surrounding the top of the borehole. The simple adjustment for mass in the middle panel yields results with an exposure duration and erosion rate that are inconsistent (considerably higher) with those derived from the surface sample.

6.2 Orbital-scale erosion

We assess the potential for using bedrock cores in proglacial settings to constrain the magnitude of subglacial erosion over multiple timescales. Here, we explore the effects of both short- and long-term subglacial erosion on ^{10}Be depth profiles in bedrock. We demonstrate that modeling erosion rates through the Pleistocene yields realistic estimates of recent erosion, as well as constraints on subglacial erosion rates on orbital timescales at the same location.

6.2.1 Excess muon-produced ^{10}Be at depth

To evaluate subglacial erosion at the bedrock core site, we first compare our measured ^{10}Be concentrations with depth to the theoretical ^{10}Be production curve with depth (i.e., Schaefer et al., 2016). In the upper ~2 m of the rock column, the measured ^{10}Be concentrations are congruent with the predicted concentrations (Figure 6). However, below ~2 m, our measured ^{10}Be concentrations consistently exceed the predicted ^{10}Be concentrations, yielding a poor fit to the data overall (χ^2 = 7.45; Figure 6). In other words, below ~2 m depth the e-folding length of our measured ^{10}Be concentrations is greater than the attenuation length of ^{10}Be production at those depths (i.e., ^{10}Be decreases more slowly with depth than expected).

To simulate subglacial erosion during the most recent period of ice cover, we assume that the modern bedrock surface was covered by some additional mass (presumably rock) when the core site was first exposed during the Holocene and determine the erosional depth by adjusting how far the bedrock was below the modern surface when the measured ^{10}Be accumulated (Schaefer et al., 2016). Using this method, we find a good model-data fit ($\chi^2 = 1.77$; Figure 6); however, the best-fitting curve implies an exposure duration of ~15 kyr, and an erosional depth of ~50 cm (Figure 6). These results are seemingly realistic for postglacial landscapes that lack independent constraints on the exposure history and subglacial erosion rate, yet they are inconsistent with the known exposure duration (~7300 years during the Holocene) of the core location and the erosional depth derived from the surface sample 18JAK-CR1-SURFACE (1.30 ± 2.17 cm), which was taken from bedrock immediately surrounding the borehole. Indeed, with this

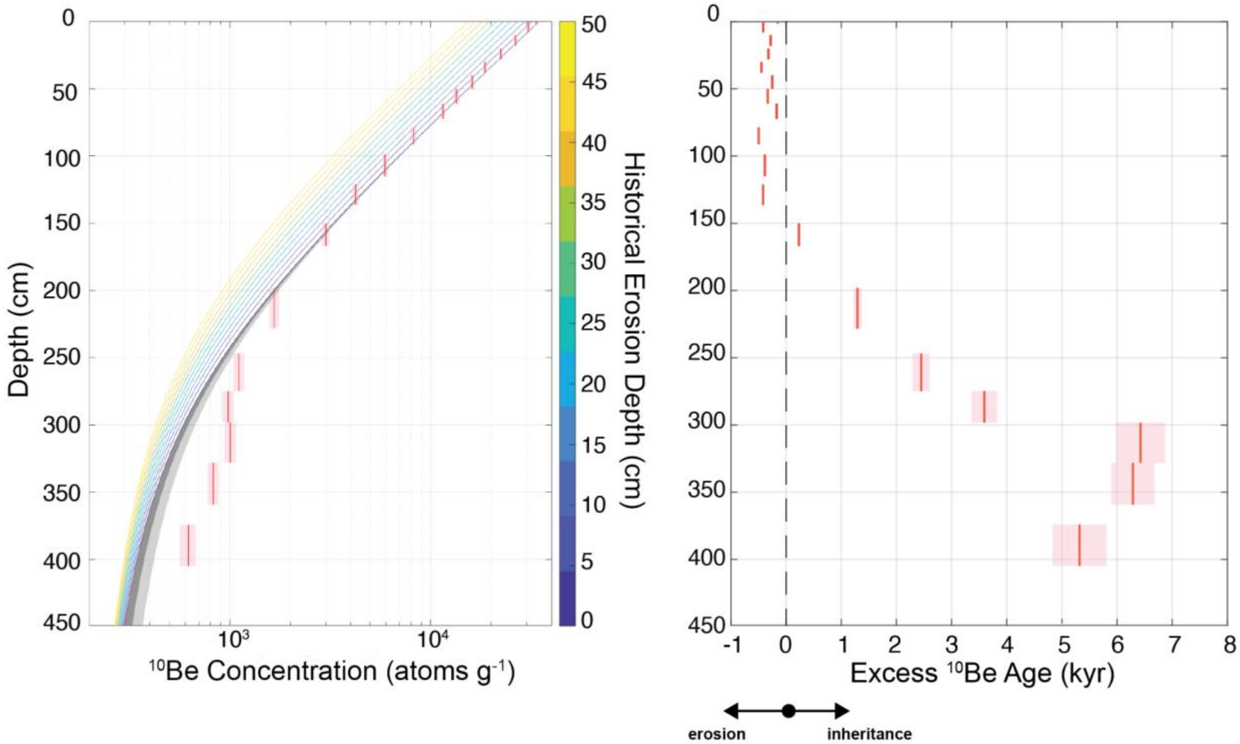

Figure 7. Measured ^{10}Be concentrations represent subglacial erosion on a range of timescales. **Left:** ^{10}Be depth profiles modeled using the known Holocene history at the bedrock core site, with subglacial erosion of 0–50 cm during historical cover (plotted every 5 cm). Note that a higher degree of subglacial erosion effectively "truncates" the ^{10}Be depth profile from the top. Measured ^{10}Be concentrations in the bedrock core are plotted in red, and are most consistent with ~0–10 cm of erosion during historical cover. However, measured ^{10}Be below ~2 m depth exceeds modeled ^{10}Be in all scenarios. Dark grey envelope is 10% uncertainty in the muon production rate and light gray envelope is 25% muon uncertainty. **Right:** measured ^{10}Be concentrations plotted as apparent exposure ages in excess of the known exposure age for the core site (~7300 years). Ages that plot to the left of zero require erosion (i.e., exposure ages are less than expected), and those that plot to the right of zero contain muon inheritance (i.e., exposure ages are greater than expected), which can be used to determine orbital-scale erosion rates. In both panels, widths of red boxes show 1σ measurement uncertainty.

fitting method it is possible to simulate ^{10}Be concentrations that match the measured concentrations at our sample depths only when using exposure durations and erosional depths that far exceed those known for our field site. While this fitting method for determining subglacial erosional depths may recover realistic results for landscapes where little is known about the glacial history, using bedrock cores to reconstruct subglacial erosion is more useful in landscapes where the exposure history has prior constraints.

Next, we derive ^{10}Be concentrations with depth using the known exposure history for this site (deglaciation 7510 years ago, 222 years of late Holocene cover, 10 years recent exposure) and varying amounts of subglacial erosion during historical cover (Figure 7). The ^{10}Be concentrations in the top ~2 m of the core fit best with ~0–10 cm of erosion during historical cover, which is statistically identical to the erosion depth derived solely from our surface measurement (erosional depth from 18JAK-CR1-SURFACE is 1.30 ± 2.17 cm). However, the ^{10}Be measurements below ~2 m depth, again, exceed those predicted by all erosion scenarios. This finding points to surplus ^{10}Be measured below ~2 m depth, even when considering uncertainty in the muon production rate of 10–25% (Balco, 2017) [at the core location, the muon production rate uncertainty is likely closer to 10% as the muon production rate was calibrated in Antarctica, another high-latitude location (Balco, pers comm)]. We also cast the measured ^{10}Be concentrations in the bedrock core as apparent exposure ages using the ^{10}Be production rate at the sample depth. When compared to the known Holocene exposure duration for the site (~7300 years), the apparent exposure ages in the upper ~1.5 m of the core are slightly less than 7300 years, implying that we measured less ^{10}Be than we expected and that some amount of recent subglacial erosion has taken place (Figure 7). In other words, recent subglacial erosion has removed ^{10}Be in the spallation-dominated part of the ^{10}Be depth profile. In contrast, the apparent ^{10}Be ages below ~1.5 m are, within error, increasingly older than 7300 years. For example, in order to get the measured concentration of ~620 atoms g^{-1} in the lowermost sample, the surface would have to have been exposed for 12,600 years, which is 5,300 years, or 70%, longer than expected. If some of this ^{10}Be accumulated when the sample was deeper in the rock column (i.e., deeper than the modern sample depth), the integrated production rate experienced by the sample would be lower, so these excess ^{10}Be ages are minima.

Excess ^{10}Be at depth represents a buildup of muon-produced ^{10}Be over many glacial cycles, which erosion (surface lowering) during glacial periods gradually brings toward the surface (Ploskey & Stone, 2014; Figure 8). This is possible because muon production (albeit low) continues to all depths in rock, so even high subglacial erosion rates are often insufficient to remove the muon signature of previous exposure periods (e.g., Briner et al., 2016). Therefore, all rock surfaces likely contain some muon-produced ^{10}Be inherited from prior exposure periods. Yet, in many settings inherited ^{10}Be from muon production is well below the measurement detection limit, meaning that a sample at the surface yields a ^{10}Be concentration commensurate with its exposure age. No newly exposed bedrock surface would have a ^{10}Be concentration of zero, but the inherited muon-produced ^{10}Be concentration in a surface sample is often within measurement error. Given the abundance of inherited muon-produced ^{10}Be at depth, recent and long-term subglacial erosion are differentially recorded in ^{10}Be depth profiles. The spallation-dominated upper ~2–3 m of the depth profile is sensitive to recent subglacial erosion, as ^{10}Be concentrations near the surface decrease rapidly with depth. In contrast, the ^{10}Be concentration below ~2–3 m, where muon interactions comprise the majority of production, is increasingly less sensitive to recent erosion because the ^{10}Be concentrations (albeit generally low) decrease slowly with depth. Therefore, muon-produced ^{10}Be inherited from prior periods of exposure becomes increasingly important with depth in rock below the modern surface (Figure 8). This combination results in the spallation-dominated portion of the depth profile recording recent subglacial erosion, while the build-up of muon-produced ^{10}Be records the long-term average erosion rate (i.e, orbital timescales). Not only does this inherited muon-produced ^{10}Be allow for evaluation of long-term erosion rates (Ploskey & Stone, 2014), but failing to incorporate it into our analysis of the bedrock core data at Jakobshavn Isbræ leads to erroneous results for the historical erosion rate (Figure 6).

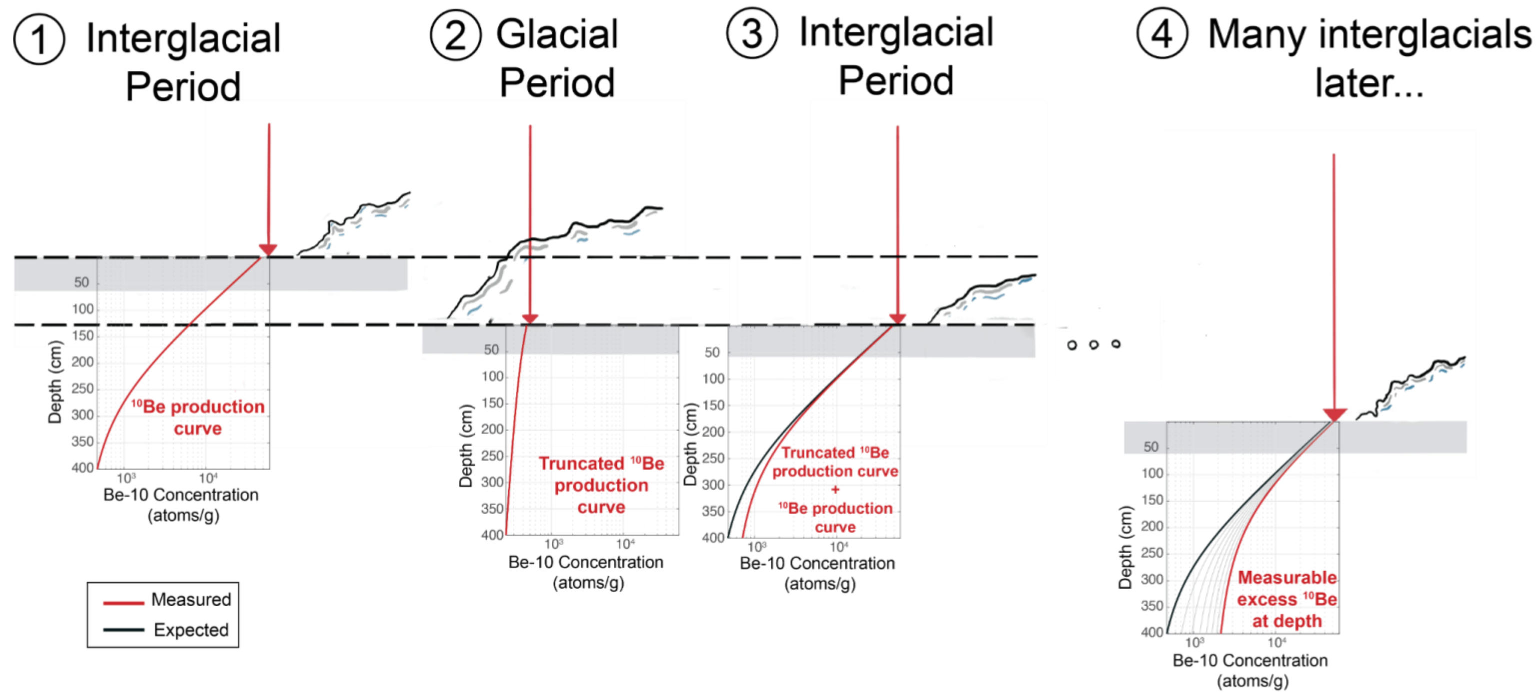

Figure 8. Cartoon showing how excess ^{10}Be builds up at depth over many glacial cycles [concept adapted from Ploskey & Stone (2014)]. Each panel shows the same bedrock coring location (red arrow) and associated ^{10}Be depth profiles at different points throughout several glacial cycles. The black depth profiles show the expected the ^{10}Be concentration based on the ^{10}Be production curve, and red depth profiles show the ^{10}Be concentration that would be measured at the end of each period represented by that panel. **1)** At the end of the first exposure (interglacial) period, the measured ^{10}Be depth profile will look like the ^{10}Be production profile. **2)** During the following burial (glacial) period, subglacial erosion takes place, removing ^{10}Be from the top down. At the end of the glacial period, the ^{10}Be depth profile will appear truncated according to how much erosion took place. **3)** During a subsequent exposure (interglacial) period, ^{10}Be will again accumulate with the shape of the ^{10}Be production profile (black). At the surface, where production is spallation-dominated, this new production would overpower any ^{10}Be leftover from the last glacial cycle. At depth, however, where ^{10}Be production is low and muon-dominated, the leftover ^{10}Be from the previous glacial period becomes important. **4)** Over many glacial cycles, this muon-produced ^{10}Be from previous exposure periods builds up and, while generally overpowered by the most recent spallation signal at the surface, causes there to be measurable excess ^{10}Be at depth. Therefore, excess ^{10}Be only occurs after at least one period of erosion from the surface. For the sake of illustration, the glacial periods used to create this cartoon are 90 kyr, the interglacial periods are 10 kyr, and 4 m of erosion takes place during each glacial period. In reality, the amount of excess ^{10}Be at depth is dependent on the erosional depth (rate) during glacial periods.

6.2.2 Quantifying orbital- and centennial-scale erosion rates from a bedrock core

Here, we model cosmogenic-nuclide build-up to invert the 17 measured ^{10}Be concentrations in our 4-m-long bedrock core for the best estimate of centennial- and orbital-scale erosion rates at the coring location. To do so, we model ^{10}Be concentrations with depth in bedrock through the Pleistocene for a range of exposure histories and subglacial erosion rates using the model framework described below. To determine the best-fitting erosion rates for each combination of exposure history, historical subglacial erosion rates and Pleistocene subglacial erosion rates, we used the reduced chi-squared statistic, which is weighted using the measurement uncertainty in the ^{10}Be concentrations.

In our model, cosmogenic ^{10}Be accumulates when the bedrock core site is ice free and subglacial erosion occurs when the site is ice covered. The two free parameters in our model are the historical subglacial erosion rate and the Pleistocene (pre-Holocene) subglacial erosion rate. The Pleistocene erosion rate is kept constant for all Pleistocene burial periods, and therefore is considered to be an average Pleistocene erosion rate. The exposure history (nuclide accumulation) and the subglacial erosion rate (nuclide removal) ultimately determine the ^{10}Be concentration at the end of the model run, and infinite combinations of these parameters can yield the same ^{10}Be concentration (i.e., more exposure during the Pleistocene would require higher erosion rates to arrive at the same ^{10}Be concentration). Therefore, the exposure history that we select to drive the model determines what erosion rates will yield ^{10}Be concentrations that best fit our measurements. An advantage of using the bedrock fronting Jakobshavn Isbræ is that the Holocene ice-margin history is well constrained, meaning that unique erosion rate results are possible for historical ice cover. The pre-Holocene glacial history of our study area, however, is unconstrained, so we use the δ^{18}O of marine calcite as a proxy for the exposure history at our bedrock core location. To determine the exposure/burial history at our core site, we implemented threshold $\delta^{18}O$ values on the marine benthic $\delta^{18}O$ LR04 stack (Lisiecki and Raymo, 2005; 30 kyr smoothing) to determine plausible exposure histories of the site prior to the Holocene (Knudsen et al., 2015; we ran our model for exposure histories derived from $\delta^{18}O$ thresholds of 3.3–4.0‰). For the Holocene, we used the known ice-margin history described in Section 5 to drive the model (deglaciation age = 7510 ka, historical ice cover = 213 years, 10 years of recent exposure prior to sampling).

We compute the ^{10}Be production rate with depth as described in Sections 3.3 and 3.4, but here use "St" scaling of Lal (1991) / Stone (2000). Although we do not implement time-variant scaling methods, the use of such a method would yield nearly identical ^{10}Be concentrations for the Holocene, the only time period for which we expect to have remaining spallation-produced ^{10}Be at the core site, because the production rate we employ was calibrated locally (Young et al., 2013a). Finally, while the elevation of the Earth's surface at the core site cannot be known through the Pleistocene, muon interactions, which account for the production of ^{10}Be preserved on glacial-interglacial timescales, are less sensitive to changes in the surface elevation than spallation reactions because of the longer attenuation length of muons traveling through the atmosphere.

We assume that the core location was ice free prior to the model start and that the bedrock began with an ^{10}Be inventory in steady state (i.e., nuclide production is balanced by nuclide loss from decay and erosion). We initialize the model with steady-state ^{10}Be concentrations using subaerial erosion rates of 5 m Myr^{-1}, 10 m Myr^{-1}, and 50 m Myr^{-1}. Note that the starting depths of our samples are >100 m for our best-fitting model runs (Table 3), meaning that starting ^{10}Be concentrations are extremely low even with the initial steady state conditions.

To assess the importance of the steady state starting conditions, we also run the model with a starting ^{10}Be concentration of zero, although this assumption is unrealistic given that the site would have been exposed prior to the first period of ice cover. Model time begins either at 2.7 Ma (beginning of the Pleistocene), or with the first burial period after 2.7 Ma if the δ^{18}O is below the threshold (i.e., site is ice free) at the beginning of the Pleistocene.

Model time runs towards the present with the length of each exposure/burial period determined by the δ^{18}O threshold. Nuclide accumulation is quantified during exposure using the equation,

$$N_{new} = N_{old} * e^{-\lambda * t_{exp}} + \frac{P(z)}{\lambda} * (1 - e^{-\lambda * t_{exp}})$$

where N_{new} is the ^{10}Be concentration at the end of the time step (in this case, exposure period), N_{old} is the ^{10}Be concentration at the start of the time step, λ is the ^{10}Be decay constant (4.99 x 10^{-7} yr^{-1}; Chmeleff et al., 2010; Korschinek et al., 2010), t_{exp} is the exposure duration for that time step, and *P(z)* is the total ^{10}Be production rate (spallation + muon) at the depth *z* in rock. Subaerial erosion during interglacial periods is not included in this version of our model, but is thought to be extremely low in this region. During the current interglacial, well preserved striations and glacial polish between the mouth of Jakobshavn Isfjord (deglaciated ~10.2 ka) and the historical moraine are evidence for extremely low subaerial erosion rates (Young et al., 2011). Furthermore, subaerial erosion rates derived using cosmogenic-nuclide analysis on tors on Baffin Island at a similar latitude to our fieldsite suggest subaerial erosion rates are <2 mm ka^{-1} (Margreth et al., 2016).

When the site is ice covered, nuclide decay continues following,

$$N_{new} = N_{old} * e^{-\lambda * t_{bur}}$$

where t_{bur} is the burial duration for that time step. During each burial period, we also simulate subglacial erosion by advecting the depth profile towards the surface (i.e., moving the depth profile up in the rock column) according to the prescribed erosion rate and burial duration. The modeled depth profile then begins the next exposure period at an updated ^{10}Be production rate commensurate with its new depth below the earth's surface.

In sum, we model cosmogenic ^{10}Be concentrations through the Pleistocene with two free parameters: the pre-Holocene subglacial erosion rate and the historical subglacial erosion rate. For the Holocene, we use the known exposure history at the bedrock core location, and we test a range of Pleistocene exposure histories calculated using threshold values on the benthic δ^{18}O stack of Lisiecki & Raymo (2005). Ultimately, we invert for the best-fitting erosion rates using the reduced chi-squared statistic to recover centennial- and orbital-scale subglacial erosion rates at our bedrock core location.

6.2.3 Modeled orbital- and centennial-scale erosion rates

Some combination of historical and long-term erosion rates yields a good model-data fit for each exposure history we modeled (determined using threshold values on the δ^{18}O curve of 3.3–4.0‰) (Figure 9; Figure 10). With the exception of the histories derived using δ^{18}O thresholds of 3.3 and 3.4‰, historical abrasion rates are consistent across exposure histories (~0.2 mm yr^{-1}), and long-term erosion rates increase with increasing cumulative exposure duration during the Pleistocene (Figure 10). As with the surface samples, we consider the historical erosion rate to be an abrasion rate because we selected a coring site with evidence of abrasion only; however, we consider the Pleistocene erosion rate to be a total erosion rate as both abrasion and quarrying likely took place at this site over the course of the Pleistocene.

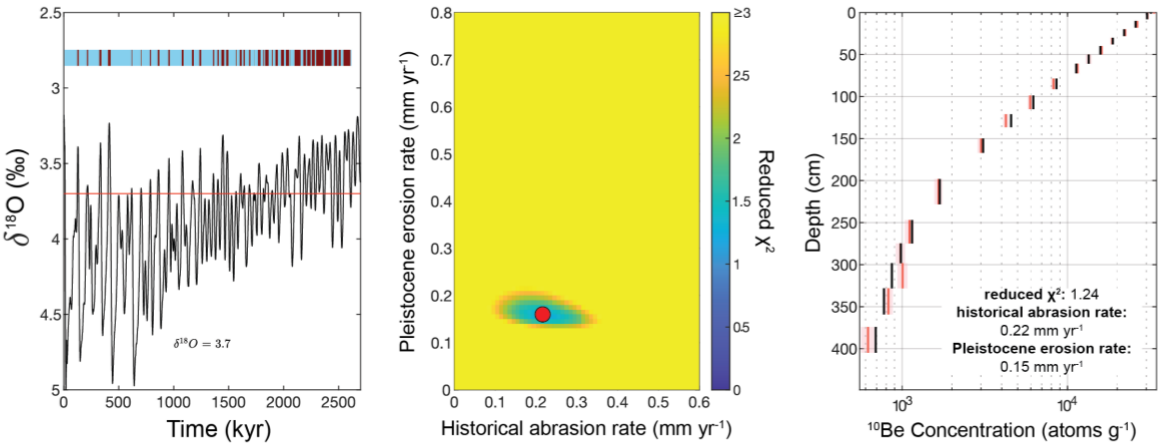

Figure 9. Best-fitting centennial- and orbital-scale erosion rates for the glacial history determined using a δ^{18}O threshold of 3.7‰, the known glacial history for the Holocene (Section 5), and an initial steady-state erosion rate of 5 m Myr^{-1}. **Left:** Benthic δ^{18}O stack (Lisiecki and Raymo, 2005) with horizontal red line showing threshold value for this model run. Glacial history at the core site shown in the bar at the top of the figure, where blue is times the core site is ice covered (erosion) and red is times the site is exposed (nuclide accumulation). **Middle:** Misfit of modeled ^{10}Be depth profiles to measured ^{10}Be concentrations using different combinations of historical and orbital-scale subglacial erosion rates. The best-fitting combination of Pleistocene and historical erosion rates is shown at the red circle. **Right:** Modeled best-fitting ^{10}Be concentrations at the core sample depths (black) and the measured ^{10}Be concentrations of the core samples (red). Widths of red boxes show 1σ measurements uncertainty. The reduced χ^2 statistic, historical abrasion rate, and orbital-scale erosion rate of the best-fitting scenario are shown in text within the figure. In the best-fitting scenario, modeled ^{10}Be concentrations are consistent with the measured ^{10}Be concentrations at all depths and the historical abrasion rate is comparable to that determined from the surface sample 18JAK-CR1-SURFACE.

Examining results from the model runs with δ^{18}O thresholds of 3.3 and 3.4‰ further elucidates the role of excess muon-produced ^{10}Be in influencing recent subglacial erosion rate results. In the exposure histories determined using 3.3 and 3.4‰ δ^{18}O thresholds there is little pre-Holocene exposure, and therefore less ^{10}Be produced throughout the rock column during the Pleistocene. Similar to the curve-fitting exercises described in Section 6.2.1 (Figure 6), a good fit to the data is only achieved when a higher amount of recent erosion is invoked because there is not enough build-up of muon-produced ^{10}Be at depth. In other words, the inherited muon-produced ^{10}Be we know to be present at the site increases the e-folding length of the measured ^{10}Be depth profile, so the modeled depth profiles that fit the data imply that our samples were deeper in the rock column when the measured ^{10}Be accumulated. Ultimately, the 3.3 and 3.4‰ thresholds do not provide enough Pleistocene exposure to account for the excess muon-produced ^{10}Be observed in the measured concentrations unless we invoke a near-zero Pleistocene erosion rate and a likely too-high historical abrasion rate of ~0.5 mm yr^{-1}.

In contrast, the exposure histories from δ^{18}O thresholds between 3.5 and 4.0‰ yield a remarkably consistent historical abrasion rate (~0.2 mm yr^{-1}) and a long-term erosion rate that increases with greater cumulative exposure (increasing threshold value) during the Pleistocene (Figure 10). This historical abrasion rate is remarkably consistent with the abrasion rate determined using surface sample 18JAK-CR1-SURFACE (0.06 ± 0.11 mm yr^{-1}). Indeed, the slightly higher historical abrasion rate recovered from the bedrock core may be more realistic than that from the surface sample, as our inverse modeling exercise accounts for the small amount of inherited muon-produced ^{10}Be present even at the bedrock surface. The presence of inherited muon-produced ^{10}Be at the bedrock surface also has implications for the generating apparent exposure ages at and beyond Jakobshavn Isbræ. For example, in southwestern Norway, a setting with long ice-free periods during glacial cycles, apparent exposure ages from erratic boulders are, on average, ~10% older than a basal radiocarbon age on a downflow marine sediment core, which can be perhaps explained by the presence of inherited muon-produced ^{10}Be in the boulders (Briner et al., 2016). Surprisingly, even at Jakobshavn Isbræ, a setting thought to have negligible inheritance (i.e., exposure ages from surficial bedrock samples are statistically identical to local radiocarbon chronologies from proglacial-threshold lakes), we observed inherited muon-produced ^{10}Be at depth. The inherited component of the lowest bedrock core sample is <1% of the ^{10}Be concentration at the surface, a value less than measurement error in our surface sample and therefore undetectable. Even in places where the inherited muon-produced ^{10}Be comprises a larger fraction of the surface concentration, use of a locally calibrated ^{10}Be production likely counteracts the overall effect of inheritance on the chronology. Here, the production rate we use for calculating apparent exposure ages was calibrated using samples just down-fjord from our field site (Young et al., 2013a), which likely contain a similar amount of inherited muon-produced ^{10}Be as these calibration samples were likely sourced from the same bedrock terrain (i.e. same long-term exposure and burial history). When calculating exposure ages, the inherited muon-produced ^{10}Be in the calibration data offsets the inherited component of our surface samples of unknown age, so the deglaciation chronology presented here is likely unaffected by inheritance. Nevertheless, identifying an inherited muon component at depth highlights the potential for using bedrock cores to identify inherited nuclides that lead to spurious glacial chronologies.

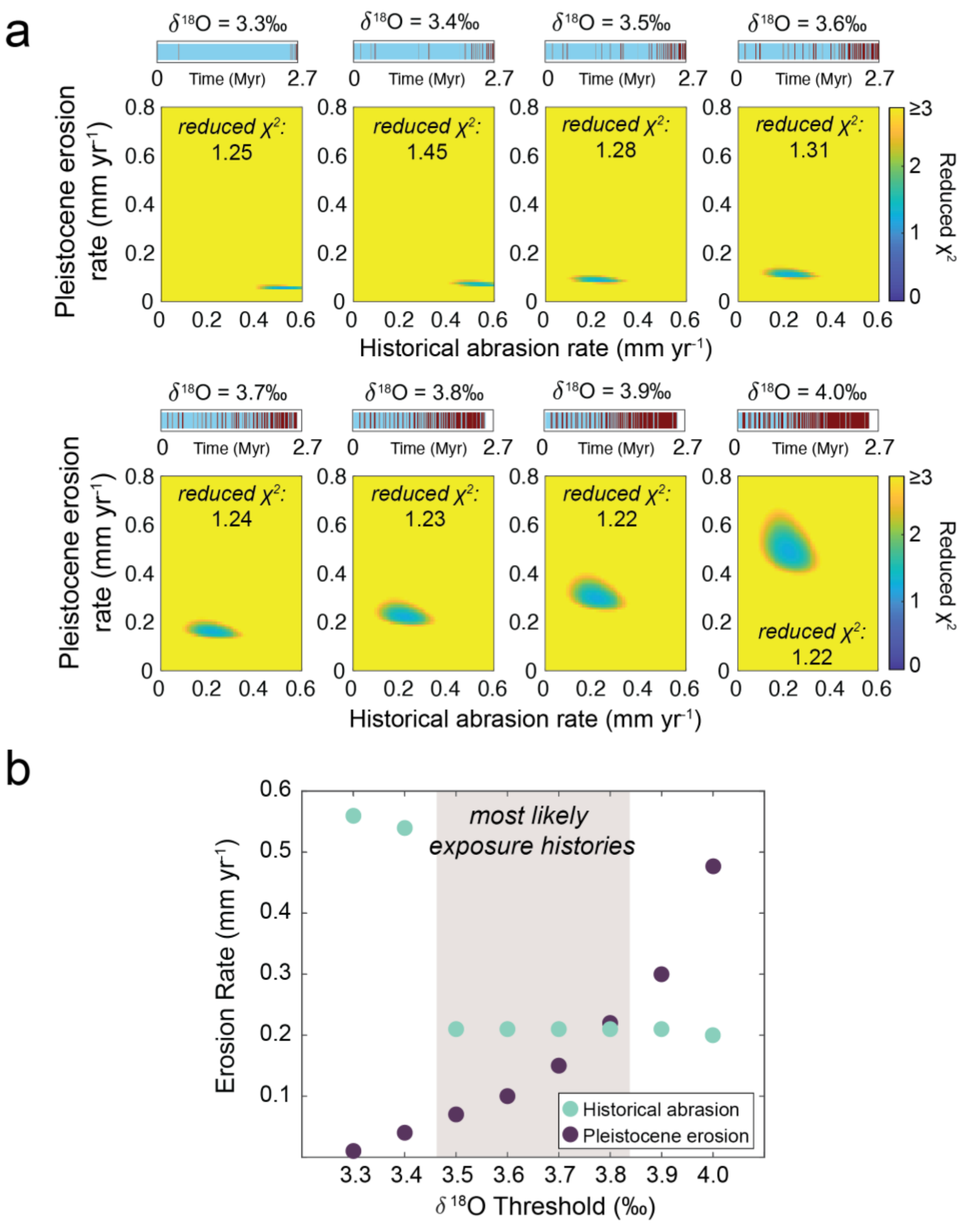

Figure 10: Best-fitting erosion rates for glacial histories determined using $\delta^{18}O$ thresholds of 3.3–4.0‰, the known glacial history for the Holocene (Section 5), and an initial steady-state erosion rate of 5 m Myr^{-1}. Model runs with initial steady-state erosion rates of 10 and 50 m Myr^{-1} are nearly identical and shown in Figure S1. **a)** Glacial history at the core site shown in the bar at the top of each figure, where blue is times the core site is ice covered and red is times the site is exposed. The color maps show the misfit of modeled ^{10}Be depth profiles to measured ^{10}Be concentrations using different combinations of historical abrasion and orbital-scale subglacial erosion rates for each of the glacial histories. The reduced χ^2 statistic of each best-fitting scenario is shown in text within each figure. **b)** Scatter plot of the best-fitting Pleistocene erosion and historical abrasion rates for each $\delta^{18}O$ threshold, with the $\delta^{18}O$ thresholds yielding the most plausible glacial histories shown within the gray box.

In the exposure histories derived using $\delta^{18}O$ thresholds between 3.5 and 4.0‰, higher erosion rates throughout the Pleistocene offset more Pleistocene exposure to capture excess (higher-e-folding length) ^{10}Be at depth, but the best-fitting historical abrasion rate is constrained by the known Holocene glacial history. In other words, there is enough Pleistocene exposure to simulate inherited muon-produced ^{10}Be below ~2 m depth without relying on an unrealistically high historical erosion rate to replicate that excess ^{10}Be. The historical erosion rate therefore is constrained by the known Holocene ice-margin history, where too-low (too-high) erosion rates yield too-high (too-low) modeled ^{10}Be concentrations in the upper ~2 m when compared with our measurements. Overall, unlike with the $\delta^{18}O$ thresholds of 3.3 and 3.4‰, using a $\delta^{18}O$ threshold of 3.5–4.0‰ simulates the excess ^{10}Be with depth that we observe with our measured ^{10}Be concentrations from the bedrock core.

The long-term erosion rate that best fits the measured ^{10}Be concentrations in our bedrock core is directly related to the duration of exposure during the Pleistocene, as more (less) exposure requires higher (lower) subglacial erosion rates to produce modeled ^{10}Be concentrations that match the measured data. Although the Holocene exposure history at our core location is precisely known, little is known about pre-Holocene configurations of Jakobshavn Isbræ and, more broadly, the GrIS margin. Nevertheless, we can determine which of our employed $\delta^{18}O$ thresholds yields the most plausible glacial histories for our site given broad constraints on GrIS configurations throughout the Pleistocene and ultimately narrow down the range of possible orbital-scale subglacial erosion rates at Jakobshavn Isbræ.

We first compared the amount of modeled exposure during the Last Interglaciation in each of our model runs to what is known about the likely duration of MIS 5e exposure along the western GrIS. Triple cosmogenic-nuclide measurements (^{14}C-^{26}Al-^{10}Be) from the Nuuk region indicate that ~10–15 kyr of inheritance is present in the surficial bedrock at several ice-marginal locations that also deglaciated during historical times; based on the $^{26}Al/^{10}Be$ concentrations at these locations, this excess exposure most likely comes from MIS 5e (Young et al., 2021). The exposure histories for our core site derived using $\delta^{18}O$ thresholds of 3.3‰ (zero exposure during the Last Interglacial) and 3.4‰ (3 kyr exposure during the Last Interglacial from 131–129 ka), likely have too little exposure during the Last Interglacial, while the history associated with the $\delta^{18}O$ threshold of 4.0‰ (53 kyr exposure during the Last Interglacial and into the last glacial period), likely has too much, although not impossible, exposure during the last glacial cycle (Table 3). In contrast, $\delta^{18}O$ thresholds between 3.5–3.9‰ yield plausible exposure durations at our field site during MIS 5e (7–19 kyr; Table 3).

Cosmogenic-nuclide studies that have implications for the general Pleistocene exposure history in Greenland corroborate that the 3.3 and 3.4‰ $\delta^{18}O$ thresholds yield histories that likely have too little exposure during the Pleistocene. Strunk et al. (2017) used multiple cosmogenic isotopes to suggest that sample locations in western Greenland positioned similarly to our site (i.e., low elevation, adjacent to fast flowing ice streams) were perhaps exposed for ~60% of the last million years. Although our model considers the entire Pleistocene, the histories associated with $\delta^{18}O$ thresholds of 3.3 and 3.4‰ indicate ice-free conditions at the core site only 2% and 6% of the Pleistocene, respectively, which is probably too little exposure (Table 3). Finally, ^{10}Be concentrations from a bedrock core from beneath the GrIS at the GISP2 site, at the center of the ice sheet, likely equate to ~200–280 kyr of cumulative exposure during the Pleistocene (Schaefer et al., 2016). Our bedrock core location at the margin of the GrIS must have experienced more cumulative surface exposure than an interior site such as GISP2, yet histories derived using $\delta^{18}O$ thresholds of 3.3 and 3.4‰ have only 44 and 166 kyr exposure, respectively (Table 3). Given this sparse knowledge of pre-Holocene configurations of the GrIS, we suggest that the histories associated with $\delta^{18}O$ thresholds of 3.5–3.9‰ are most plausible for our core location at Jakobshavn Isbræ. The best-fitting orbital-scale erosion rates for these exposure histories are between 0.1–0.3 mm yr^{-1} (denudation rate of 70–140 m Myr^{-1}) (Figure 10; Table 3). The historical abrasion rates recovered from this modeling effort (0.2 mm yr^{--1}) scales to a total erosion (abrasion + quarrying) rate of 0.3–0.5 mm yr^{-1}, which is in agreement with the erosion rate derived from the surface samples of 0.4–0.8 mm yr^{-1}.

Down-core ^{10}Be measurements in proglacial bedrock cores are a novel tool for directly quantifying subglacial erosion rates. Using simulations of ^{10}Be accumulation/decay and subglacial erosion through the Pleistocene, we are able to replicate centennial-scale subglacial erosion rates determined from surficial bedrock samples. Furthermore, concentrations of inherited ^{10}Be below ~2 m depth provide plausible orbital-scale subglacial erosion rates at Jakobshavn Isbræ. When using this method in proglacial settings, known constraints on the glacial history are useful for recovering the most accurate erosion rates. Failing to account for the build-up of muon-produced ^{10}Be at depth by including a Pleistocene history with sufficient cumulative exposure leads to spuriously high recent (historical) erosion rates (Sections 6.1.1 and 6.1.2). Furthermore, our findings indicate that collecting bedrock cores that are ≥4 m depth is required to sufficiently capture the inherited muon-produced component needed for orbital-scale simulations; in cores <4 m, the inherited muon component could be obscured by ^{10}Be that more recently accumulated. To further explore the constraints and applications of this method, future model iterations could include multiple cosmogenic nuclides (e.g., ^{26}Al, ^{36}Cl, and ^{14}C), subaerial erosion during intervals of surface exposure in regions where subaerial erosion might be significant, and variable subglacial erosion rates through intervals of ice cover. Nevertheless, with our current model, we demonstrate that the use of bedrock cores in proglacial settings unlocks new applications for using muon-produced cosmogenic nuclides as a means for quantifying both short- and long-term subglacial erosion rates.

Table 3 - Information about glacial history inputs to cosmogenic-nuclide model for bedrock core 18JAK-CR1 and erosion outputs.

δ^{18}O threshold value used in Pleistocene erosion model (‰)	Model Start Time (kyr)[1]	Total Pleistocene Burial (kyr)	Total Pleistocene Exposure (kyr)	Exposure During MIS 5e (kyr)	Years Exposed During 5e (ka)	Total Erosion Since Model Start (m)	Pleistocene Glacial Erosion Rate (mm/yr)[3]	Pleistocene Glacial Erosion Rate (m/Myr)[4]	Pleistocene Denudation Rate (m/Myr)[5]	Historical Abrasion Rate (mm/yr)[6]	Historical Erosion Rate (mm/yr)[7]
3.3	2700	2654	44	0	--	130	0.05	50	50	0.52	0.7–1.3
3.4	2700	2526	166	3	131–128	150	0.06	60	60	0.55	0.8–1.4
3.5	2700	2332	360	7	133–126	190	0.08	80	70	0.23	0.4–0.6
3.6	2700	2110	582	10	134–124	230	0.11	110	90	0.21	0.3–0.5
3.7	2616	1809	799	13	135–122	270	0.15	160	100	0.22	0.3–0.6
3.8	2542	1446	1088	16	136–120	320	0.22	220	130	0.21	0.3–0.5
3.9	2539	1207	1324	19 [2]	137–118; 109–103	350	0.29	300	140	0.22	0.3–0.6
4	2535	938	1589	53 [2]	138–85	450	0.48	500	180	0.22	0.3–0.6

[1]Model start time is no earlier than the beginning of the Pleistocene (2.7 Ma), but begins at the first burial.

[2]For the exposure history derived using a δ^{18}O threshold of 3.9‰, there is also 6 kyr of exposure during MIS 5c. The exposure history determined using a δ^{18}O threshold of 4.0‰ has 53 kyr total exposure across MIS 5.

[3]Best-fitting Pleistocene erosion rate from model described in section 6.2.2.

[4]Best-fitting Pleistocene erosion rate from model scaled up to m/Myr.

[5]Total erosion since model start divided by model start time. For comparison to other studies that report a total denudation rate.

[6]Best-fitting historical abrasiom rate from model described in section 6.2.2.

[7]Best-fitting historical erosion rate, scaled up from abrasion rate to include the effects of quarrying.

6.3 Comparison to other erosion rate estimates

Empirical evidence constrains subglacial erosion rates in polar climates to ~0.01–0.1 mm yr^{-1} (Hallet et al., 1996; Koppes et al., 2015). In east Greenland, sediment flux data yield a canonical Greenland erosion rate of 0.01–0.04 mm yr^{-1} (Andrews et al., 1994), which Cowton et al. (2012) revised to 0.3 mm yr^{-1} after accounting for sediment entrained in iceberg mélange after Syvitski et al. (1996). Suspended sediment and solute data from the Watson proglacial river near Kangerlussuaq in central-west Greenland constrain average subglacial erosion to 0.5 mm yr^{-1} for the years 2006–2016 (Hasholt et al., 2018), although individual years were perhaps as high as 4.5 mm yr^{-1} (Hogan et al., 2020). Furthermore, suspended sediment load from an individual glacier within the Watson River catchment yielded a higher erosion rate of 4.8 ± 2.6 mm yr^{-1} from 2009–2010 (Cowton et al., 2012). At the Petermann Glacier in northwest Greenland, the thickness of glaciomarine deposits emplaced during the last deglaciation correspond with a deglacial erosion rate of 0.29–0.34 mm a^{-1} (Hogan at al., 2020). Finally, glaciomarine facies deposited at the mouth of Jakobshavn Isfjord during an 800-year stillstand amid deglaciation in the early Holocene translate to a deglacial erosion rate at Jakobshavn Isbræ of 0.52 mm yr^{-1} (Hogan et al., 2012; Hogan et al., 2020). With the exception of the isolated higher erosion rate estimates described above, our historical (centennial-scale) erosion rate of ~0.3–0.8 mm yr^{-1} (abrasion + quarrying; full range encompassed by surface sample and bedrock core results) is consistent with these modern to millennial-scale estimates from Greenland. Notably, these erosion rate estimates in western Greenland are from periods when temperatures were either warm (interglacial) or warming, a factor associated with higher erosion rates owing to increased basal sliding and meltwater flux to the bed (Alley et al., 2019).

Even fewer erosion rate estimates exist for Greenland prior to the last deglaciation. Goehring et al. (2010) estimate an erosion rate of 2–34 m of erosion during the last glacial period using ^{10}Be depth profiles in raised marine and lacustrine deposits in the Scoresby Sund region, east Greenland, which scales to tens to hundreds of meters of subglacial erosion at this location since the start of the Pleistocene. In western Greenland, Strunk et al. (2017) use the lack of inherited ^{10}Be in some surficial bedrock samples to suggest that >50 m Myr^{-1} of denudation must have taken place during the Pleistocene. Finally, Corbett et al. (2021) posit that cobbles emerging directly from the GrIS in western Greenland were sourced from deeply eroded interior landscapes that, at minimum, experienced ~20–50 m Myr^{-1} erosion over the Pleistocene. Although we calculated our Pleistocene erosion rates in mm yr^{-1} for ease of comparison with the centennial scale erosion rate, when considered on the timescale of millions of years, our Pleistocene denudation rate estimate is ~70–140 m Myr^{-1} (Table 3). Our long-term erosion rate is consistent with these previous estimates, but provides more specificity in that it does not rely on a lack of inheritance (which gives a minimum estimate) but rather on the presence of inherited muon-produced ^{10}Be that holds direct information about erosion rates on orbital timescales.

7 Are centennial- and orbital-scale erosion rates the same near Jakobshavn Isbræ?

In comparing erosion rates across millions-of-years to modern timescales, several studies have identified an apparent decrease in glacial erosion rate with increasing averaging time scale (Ganti et al., 2016; Herman et al., 2013; Koppes & Montgomery, 2009; Willenbring & Jerolmack, 2016). That is, it appears that erosion rates have increased through the late Cenozoic toward the present, with the highest erosion rates occurring today. For example, apparent erosion rates increased two- to three-fold in Alaska, the Pacific Northwest, and Patagonia on timescales from 10^7 to 10^1 years (Koppes & Montgomery, 2009). While some authors interpret this to mean that the magnitude of erosion has increased as a result of late Cenozoic cooling and concomitant glacial expansion (Herman & Champagnac, 2016), others posit that the intermittency of glacial erosional processes can explain the apparent increase (Ganti et al., 2016) as the methods used necessarily integrate erosion rates from some time in the past to the present, including times when erosion is fast, slow, and even absent.

At Jakobshavn Isbræ, *in situ* subglacial erosion rates from surface and down-core ^{10}Be measurements afford comparison of erosion rates from the same location on multiple timescales. Because our model simulates erosion only during glacial periods, our results are not biased by averaging timescale, as are methods that integrate over erosional pulses and hiatuses on long timescales (Ganti et al., 2016). In comparing our historical and long-term erosion rates at Jakobshavn Isbræ, we find that the centennial-scale erosion rate (0.3–0.8 mm yr^{-1}) is of the same magnitude as the orbital-scale erosion rate (0.1–0.3 mm yr^{-1}). We recognize that our model does not simulate variable erosion rates throughout the Pleistocene; rather, our orbital-scale erosion rate represents a Pleistocene average. Nevertheless, had a pattern of increasing erosion rates through the Pleistocene been present at Jakobshavn Isbræ, we might expect historical erosion rates to be an order of magnitude or two higher than the long-term rate. Yet, our findings do not preclude times with higher-than-average and lower-than-average erosion rates during the last ~2.7 Myr, as such variability might be expected given the degree of climate variability on these timescales (e.g., Ganti et al., 2016). The similarity between the centennial- and orbital-scale erosion rates suggests that, broadly, average erosion rates in the Jakobshavn forefield have remained relatively constant throughout the Pleistocene.

Although in apparent disagreement, the relatively uniform erosion rates across the Pleistocene derived from our bedrock core and the increasing erosion rates implied by sediment flux records might actually be compatible when considering the evolution of glaciated landscapes. Our measurements are from a low-relief, interfjord plateau, whereas sediment-flux-derived erosion rates likely bias towards erosion within fjords. Interfjord plateaus like the one we sampled are thought to result from either selective linear erosion (Jamieson et al., 2014; Sugden, 1978) or feedbacks between erosion, ice dynamics, topography, and glacial-isostatic adjustment (Egholm et al., 2017). In these respective frameworks, subglacial erosion rates over interfjord plateaus are either expected to remain uniformly low, or even decrease through the Pleistocene (Egholm et al., 2017). In contrast, landscape evolution modeling shows that fjord development over the Pleistocene initiated positive feedbacks between topographic steering, ice thickening, and faster ice flow that enhanced erosion within valleys, resulting in increased erosion with successive glaciations (e.g., Kessler et al., 2008), which is consistent with empirical measurements biased towards erosion in fjords. On first order, this comparison provides empirical evidence for the theoretical feedbacks that create fjords and otherwise preserve topography in glaciated landscapes.

8 Conclusions

New ^{10}Be measurements in bedrock fronting Jakobshavn Isbræ afford direct constraints on centennial- and orbital-scale erosion rates. Erosion rates calculated from twenty ^{10}Be measurements in surficial bedrock represent an overall abrasion rate of 0.31 ± 0.34 mm yr^{-1}, which scales to a total erosion rate (abrasion + quarrying) of 0.4–0.8 mm yr^{-1} for historical times. Fourteen surficial bedrock samples with significantly younger apparent ^{10}Be ages were likely covered by sediment during the middle Holocene that was later removed during the interval of historical ice cover, experienced more Holocene ice cover, or both.

Below ~2 m depth, samples from a 4-m-long bedrock core contain excess ^{10}Be compared to an idealized cosmogenic ^{10}Be depth profile, affording quantification of subglacial erosion on Pleistocene timescales. Modeling of ^{10}Be accumulation and subglacial erosion through the Pleistocene indicate that the measured ^{10}Be concentrations in our bedrock core are most consistent with a historical erosion rate of 0.3–0.5 mm yr^{-1}, in agreement with our results from the surficial bedrock samples, and an orbital-scale erosion rate of 0.1–0.3 mm yr^{-1}. Here, we demonstrate the efficacy of using ^{10}Be measurements in proglacial bedrock cores to directly quantify past subglacial erosion rates. Our results reveal that subglacial erosion rates have likely remained relatively constant through the Pleistocene near Jakobshavn Isbræ.

Acknowledgements

This work was supported in part by the NSF Arctic System Sciences Program (Award #1503959 to NEY and JMS; #1504267 to JPB) and is based upon work supported by the National Science Foundation Graduate Research Fellowship. We thank the 109th Airlift Wing of the New York National guard for transport to and from Greenland, Air Greenland for helicopter support, and CH2MHill Polar Field Services for additional logistical support. In addition, we thank Roseanne Schwartz, Jean Hanley, and Jeremy Frisch for help processing ^{10}Be samples, Brian Kennedy for help with illustration, and Greg Balco for insightful discussions.

Data Availability Statement

There are no restrictions to access for any data within this manuscript. We are in the process of submitting these data to ICE-D:Greenland (http://greenland.ice-d.org) and the NSF Arctic Data Center (https://arcticdata.io). MATLAB code for the bedrock core model is available at https://github.com/alliebalter-kennedy/BedrockCoreModel.

References

Alley, R. B., Cuffey, K. M., & Zoet, L. K. (2019). Glacial erosion: status and outlook. *Annals of Glaciology*, *60*(80), 1–13. https://doi.org/10.1017/aog.2019.38

Andrews, J. T., Milliman, J. D., Jennings, A. E., Rynes, N., & Dwyer, J. (1994). Sediment Thicknesses and Holocene Glacial Marine Sedimentation Rates in Three East Greenland Fjords (ca. 68°N). *The Journal of Geology*, *102*(6), 669–683. https://doi.org/10.1086/629711

Axford, Y., Losee, S., Briner, J. P., Francis, D. R., Langdon, P. G., & Walker, I. R. (2013). Holocene temperature history at the western Greenland Ice Sheet margin reconstructed from lake sediments. *Quaternary Science Reviews*, *59*, 87–100. https://doi.org/10.1016/j.quascirev.2012.10.024

Balco, G. (2017). Production rate calculations for cosmic-ray-muon-produced 10Be and 26Al benchmarked against geological calibration data. *Quaternary Geochronology*, *39*, 150–173. https://doi.org/10.1016/j.quageo.2017.02.001

Balco, G., Stone, J. O., Lifton, N. A., & Dunai, T. J. (2008). A complete and easily accessible means of calculating surface exposure ages or erosion rates from 10Be and 26Al measurements. *Quaternary Geochronology*, *3*(3), 174–195. https://doi.org/10.1016/j.quageo.2007.12.001

Balco, G., Stone, J. O. H., Sliwinski, M. G., & Todd, C. (2014). Features of the glacial history of the Transantarctic Mountains inferred from cosmogenic ^{26}Al, ^{10}Be and ^{21}Ne concentrations in bedrock surfaces. *Antarctic Science*, *26*(6), 708–723. https://doi.org/10.1017/S0954102014000261

Bierman, P., & Steig, E. J. (1996). Estimating rates of denudation using cosmogenic isotope abundances in sediment. *Earth Surface Processes and Landforms*, *21*(2), 125–139. https://doi.org/10.1002/(SICI)1096-9837(199602)21:2<125::AID-ESP511>3.0.CO;2-8

Bierman, P. R., Marsella, K. A., Patterson, C., Davis, P. T., & Caffee, M. (1999). Mid-Pleistocene cosmogenic minimum-age limits for pre-Wisconsinan glacial surfaces in southwestern Minnesota and southern Baffin Island: A multiple nuclide approach. *Geomorphology*, *27*(1–2), 25–39. https://doi.org/10.1016/S0169-555X(98)00088-9

Boulton, G. S. (1979). Processes of Glacier Erosion on Different Substrata. *Journal of Glaciology*, *23*(89), 15–38. https://doi.org/10.3189/S0022143000029713

Boulton, G. S. (1996). Theory of glacial erosion, transport and deposition as a consequence of subglacial sediment deformation. *Journal of Glaciology*, *42*(140), 43–62. https://doi.org/10.3189/S0022143000030525

Briner, Jason P., & Swanson, T. W. (1998). Using inherited cosmogenic 36Cl to constrain glacial erosion rates of the Cordilleran ice sheet. *Geology*, *26*(1), 3–6. https://doi.org/10.1130/0091-7613(1998)026<0003:UICCTC>2.3.CO;2

Briner, Jason P., Goehring, B. M., Mangerud, J., & Svendsen, J. I. (2016). The deep accumulation of ^{10}Be at Utsira, southwestern Norway: Implications for cosmogenic nuclide exposure dating in peripheral ice sheet landscapes: ^{10}Be in Peripheral Ice Sheet

Landscapes. *Geophysical Research Letters*, *43*(17), 9121–9129. https://doi.org/10.1002/2016GL070100

Briner, J.P., Stewart, H. A. M., Young, N. E., Philipps, W., & Losee, S. (2010). Using proglacial-threshold lakes to constrain fluctuations of the Jakobshavn Isbræ ice margin, western Greenland, during the Holocene. *Quaternary Science Reviews*, *29*(27–28), 3861–3874. https://doi.org/10.1016/j.quascirev.2010.09.005

Briner, J.P., Young, N. E., Thomas, E. K., Stewart, H. A. M., Losee, S., & Truex, S. (2011). Varve and radiocarbon dating support the rapid advance of Jakobshavn Isbræ during the Little Ice Age. *Quaternary Science Reviews*, *30*(19–20), 2476–2486. https://doi.org/10.1016/j.quascirev.2011.05.017

Brocklehurst, S. H., & Whipple, K. X. (2004). Hypsometry of glaciated landscapes. *Earth Surface Processes and Landforms*, *29*(7), 907–926. https://doi.org/10.1002/esp.1083

Brown, E. T., Brook, E. J., Raisbeck, G. M., Yiou, F., & Kurz, M. D. (1992). Effective attenuation lengths of cosmic rays producing ^{10} Be AND ^{26} Al in quartz: Implications for exposure age dating. *Geophysical Research Letters*, *19*(4), 369–372. https://doi.org/10.1029/92GL00266

Brozović, N. (1997). Climatic Limits on Landscape Development in the Northwestern Himalaya. *Science*, *276*(5312), 571–574. https://doi.org/10.1126/science.276.5312.571

Chmeleff, J., von Blanckenburg, F., Kossert, K., & Jakob, D. (2010). Determination of the 10Be half-life by multicollector ICP-MS and liquid scintillation counting. *Nuclear Instruments and Methods in Physics Research Section B Beam Interactions with Materials and Atoms*, *268*(2), 192–199. https://doi.org/10.1016/j.nimb.2009.09.012

Cohen, D., Iverson, N. R., Hooyer, T. S., Fischer, U. H., Jackson, M., & Moore, P. L. (2005). Debris-bed friction of hard-bedded glaciers. *Journal of Geophysical Research: Earth Surface*, *110*(F2). https://doi.org/10.1029/2004JF000228

Cook, S. J., Swift, D. A., Kirkbride, M. P., Knight, P. G., & Waller, R. I. (2020). The empirical basis for modelling glacial erosion rates. *Nature Communications*, *11*(1), 759. https://doi.org/10.1038/s41467-020-14583-8

Corbett, L. B., Bierman, P. R., Neumann, T. A., Graly, J. A., Shakun, J. D., Goehring, B. M., et al. (2021). Measuring multiple cosmogenic nuclides in glacial cobbles sheds light on Greenland Ice Sheet processes. *Earth and Planetary Science Letters*, *554*, 116673. https://doi.org/10.1016/j.epsl.2020.116673

Cowton, T., Nienow, P., Bartholomew, I., Sole, A., & Mair, D. (2012). Rapid erosion beneath the Greenland ice sheet. *Geology*, *40*(4), 343–346. https://doi.org/10.1130/G32687.1

Csatho, B., Schenk, T., Van Der Veen, C. J., & Krabill, W. B. (2008). Intermittent thinning of Jakobshavn Isbræ, West Greenland, since the Little Ice Age. *Journal of Glaciology*, *54*(184), 131–144. https://doi.org/10.3189/002214308784409035

Cuzzone, J. K., Morlighem, M., Larour, E., Schlegel, N., & Seroussi, H. (2018). Implementation of higher-order vertical finite elements in ISSM v4.13 for improved ice sheet flow modeling over paleoclimate timescales. *Geoscientific Model Development*, *11*(5), 1683–1694. https://doi.org/10.5194/gmd-11-1683-2018

Egholm, D. L., Jansen, J. D., Brædstrup, C. F., Pedersen, V. K., Andersen, J. L., Ugelvig, S. V., et al. (2017). Formation of plateau landscapes on glaciated continental margins. *Nature Geoscience*, *10*(8), 592–597. https://doi.org/10.1038/ngeo2980

Fabel, D., Harbor, J., Dahms, D., James, A., Elmore, D., Horn, L., et al. (2004). Spatial Patterns of Glacial Erosion at a Valley Scale Derived From Terrestrial Cosmogenic ^{10} Be and ^{26} Al Concentrations in Rock. *Annals of the Association of American Geographers*, *94*(2), 241–255. https://doi.org/10.1111/j.1467-8306.2004.09402001.x

Ganti, V., von Hagke, C., Scherler, D., Lamb, M. P., Fischer, W. W., & Avouac, J.-P. (2016). Time scale bias in erosion rates of glaciated landscapes. *Science Advances*, *2*(10), e1600204. https://doi.org/10.1126/sciadv.1600204

Goehring, B. M., Schaefer, J. M., Schluechter, C., Lifton, N. A., Finkel, R. C., Jull, A. J. T., et al. (2011). The Rhone Glacier was smaller than today for most of the Holocene. *Geology*, *39*(7), 679–682. https://doi.org/10.1130/G32145.1

Goehring, Brent M., Kelly, M. A., Schaefer, J. M., Finkel, R. C., & Lowell, T. V. (2010). Dating of raised marine and lacustrine deposits in east Greenland using beryllium-10 depth profiles and implications for estimates of subglacial erosion: DATING OF RAISED MARINE AND LACUSTRINE DEPOSITS IN EAST GREENLAND. *Journal of Quaternary Science*, *25*(6), 865–874. https://doi.org/10.1002/jqs.1380

Hallet, B. (1996). Glacial quarrying: a simple theoretical model. *Annals of Glaciology*, *22*, 1–8. https://doi.org/10.3189/1996AoG22-1-1-8

Hallet, B., Hunter, L., & Bogen, J. (1996). Rates of erosion and sediment evacuation by glaciers: A review of field data and their implications. *Global and Planetary Change*, *12*(1–4), 213–235. https://doi.org/10.1016/0921-8181(95)00021-6

Harbor, J., Stroeven, A. P., Fabel, D., Clarhäll, A., Kleman, J., Li, Y., et al. (2006). Cosmogenic nuclide evidence for minimal erosion across two subglacial sliding boundaries of the late glacial Fennoscandian ice sheet. *Ice Sheet Geomorphology - Past and Present Processes and Landforms*, *75*(1), 90–99. https://doi.org/10.1016/j.geomorph.2004.09.036

Hasholt, B., van As, D., Mikkelsen, A. B., Mernild, S. H., & Yde, J. C. (2018). Observed sediment and solute transport from the Kangerlussuaq sector of the Greenland Ice Sheet (2006–2016). *Arctic, Antarctic, and Alpine Research*, *50*(1), S100009. https://doi.org/10.1080/15230430.2018.1433789

Heisinger, B., Lal, D., Jull, A. J. T., Kubik, P., Ivy-Ochs, S., Neumaier, S., et al. (2002). Production of selected cosmogenic radionuclides by muons 1. Fast muons. *Earth and Planetary Sciences Letters*, *200*(3–4), 345–355. https://doi.org/10.1016/S0012-821X(02)00640-4

Heisinger, B., Lal, D., Jull, A. J. T., Kubik, P., Ivy-Ochs, S., Knie, K., & Nolte, E. (2002). Production of selected cosmogenic radionuclides by muons: 2. Capture of negative muons. *Earth and Planetary Sciences Letters*, *200*(3–4), 357–369. https://doi.org/10.1016/S0012-821X(02)00641-6

Herman, F., & Champagnac, J.-D. (2016). Plio-Pleistocene increase of erosion rates in mountain belts in response to climate change. *Terra Nova*, *28*(1), 2–10. https://doi.org/10.1111/ter.12186

Herman, F., Seward, D., Valla, P. G., Carter, A., Kohn, B., Willett, S. D., & Ehlers, T. A. (2013). Worldwide acceleration of mountain erosion under a cooling climate. *Nature*, *504*(7480), 423–426. https://doi.org/10.1038/nature12877

Herman, F., De Doncker, F., Delaney, I., Prasicek, G., & Koppes, M. (2021). The impact of glaciers on mountain erosion. *Nature Reviews Earth & Environment*, *2*(6), 422–435. https://doi.org/10.1038/s43017-021-00165-9

Hippe, K. (2017). Constraining processes of landscape change with combined in situ cosmogenic 14C-10Be analysis. *Quaternary Science Reviews*, *173*, 1–19. https://doi.org/10.1016/j.quascirev.2017.07.020

Hogan, K.A., Dowdeswell, J. A., & Ó Cofaigh, C. (2012). Glacimarine sedimentary processes and depositional environments in an embayment fed by West Greenland ice streams. *Marine Geology*, *311–314*, 1–16. https://doi.org/10.1016/j.margeo.2012.04.006

Hogan, Kelly A., Jakobsson, M., Mayer, L., Reilly, B. T., Jennings, A. E., Stoner, J. S., et al. (2020). Glacial sedimentation, fluxes and erosion rates associated with ice retreat in Petermann Fjord and Nares Strait, north-west Greenland. *The Cryosphere*, *14*(1), 261–286. https://doi.org/10.5194/tc-14-261-2020

Jamieson, S. S. R., Stokes, C. R., Ross, N., Rippin, D. M., Bingham, R. G., Wilson, D. S., et al. (2014). The glacial geomorphology of the Antarctic ice sheet bed. *Antarctic Science*, *26*(6), 724–741. https://doi.org/10.1017/S0954102014000212

Joughin, I., Abdalati, W., & Fahnestock, M. (2004). Large fluctuations in speed on Greenland's Jakobshavn Isbræ glacier. *Nature*, *432*(7017), 608–610. https://doi.org/10.1038/nature03130

Kessler, M. A., Anderson, R. S., & Briner, J. P. (2008). Fjord insertion into continental margins driven by topographic steering of ice. *Nature Geoscience*, *1*(6), 365–369. https://doi.org/10.1038/ngeo201

King, M. D., Howat, I. M., Candela, S. G., Noh, M. J., Jeong, S., Noël, B. P. Y., et al. (2020). Dynamic ice loss from the Greenland Ice Sheet driven by sustained glacier retreat. *Communications Earth & Environment*, *1*(1), 1. https://doi.org/10.1038/s43247-020-0001-2

Knudsen, M. F., Egholm, D. L., Jacobsen, B. H., Larsen, N. K., Jansen, J. D., Andersen, J. L., & Linge, H. C. (2015). A multi-nuclide approach to constrain landscape evolution and past erosion rates in previously glaciated terrains. *Quaternary Geochronology*, *30*, 100–113. https://doi.org/10.1016/j.quageo.2015.08.004

Koppes, M., Hallet, B., Rignot, E., Mouginot, J., Wellner, J. S., & Boldt, K. (2015). Observed latitudinal variations in erosion as a function of glacier dynamics. *Nature*, *526*(7571), 100–103. https://doi.org/10.1038/nature15385

Koppes, M. N., & Montgomery, D. R. (2009). The relative efficacy of fluvial and glacial erosion over modern to orogenic timescales. *Nature Geoscience*, *2*(9), 644–647. https://doi.org/10.1038/ngeo616

Korschinek, G., Bergmaier, A., Faestermann, T., Gerstmann, U. C., Knie, K., Rugel, G., et al. (2010). A new value for the half-life of 10Be by Heavy-Ion Elastic Recoil Detection and liquid scintillation counting. *Nuclear Instruments and Methods in Physics Research Section B: Beam Interactions with Materials and Atoms*, *268*(2), 187–191. https://doi.org/10.1016/j.nimb.2009.09.020

Lal, D. (1991). Cosmic ray labeling of erosion surfaces: in situ nuclide production rates and erosion models. *Earth and Planetary Science Letters*, *104*(2–4), 424–439. https://doi.org/10.1016/0012-821X(91)90220-C

Larour, E., Seroussi, H., Morlighem, M., & Rignot, E. (2012). Continental scale, high order, high spatial resolution, ice sheet modeling using the Ice Sheet System Model (ISSM). *Journal of Geophysical Research: Earth Surface*, *117*(F1). https://doi.org/10.1029/2011JF002140

Lisiecki, L. E., & Raymo, M. E. (2005). A Pliocene-Pleistocene stack of 57 globally distributed benthic δ^{18}O records: PLIOCENE-PLEISTOCENE BENTHIC STACK. *Paleoceanography*, *20*(1), n/a-n/a. https://doi.org/10.1029/2004PA001071

Lowry, D. P., Golledge, N. R., Bertler, N. A. N., Jones, R. S., McKay, R., & Stutz, J. (2020). Geologic controls on ice sheet sensitivity to deglacial climate forcing in the Ross Embayment, Antarctica. *Quaternary Science Advances*, *1*, 100002. https://doi.org/10.1016/j.qsa.2020.100002

Margreth, A., Gosse, J. C., & Dyke, A. S. (2016). Quantification of subaerial and episodic subglacial erosion rates on high latitude upland plateaus: Cumberland Peninsula, Baffin Island, Arctic Canada. *Quaternary Science Reviews*, *133*, 108–129. https://doi.org/10.1016/j.quascirev.2015.12.017

Morlighem, M., Rignot, E., Seroussi, H., Larour, E., Ben Dhia, H., & Aubry, D. (2010). Spatial patterns of basal drag inferred using control methods from a full-Stokes and simpler models for Pine Island Glacier, West Antarctica: SPATIAL PATTERNS OF BASAL DRAG. *Geophysical Research Letters*, *37*(14), n/a-n/a. https://doi.org/10.1029/2010GL043853

Nishiizumi, K., Imamura, M., Caffee, M. W., Southon, J. R., Finkel, R. C., & McAninch, J. (2007). Absolute calibration of 10Be AMS standards. *Nuclear Instruments and Methods in Physics Research Section B: Beam Interactions with Materials and Atoms*, *258*(2), 403–413. https://doi.org/10.1016/j.nimb.2007.01.297

Pedersen, Vivi K., Huismans, R. S., Herman, F., & Egholm, D. L. (2014). Controls of initial topography on temporal and spatial patterns of glacial erosion. *Geomorphology*, *223*, 96–116. https://doi.org/10.1016/j.geomorph.2014.06.028

Pedersen, Vivi Kathrine, & Egholm, D. L. (2013). Glaciations in response to climate variations preconditioned by evolving topography. *Nature*, *493*(7431), 206–210. https://doi.org/10.1038/nature11786

Pendleton, S., Miller, G., Lifton, N., & Young, N. (2019). Cryosphere response resolves conflicting evidence for the timing of peak Holocene warmth on Baffin Island, Arctic Canada. *Quaternary Science Reviews*, *216*, 107–115. https://doi.org/10.1016/j.quascirev.2019.05.015

Ploskey, Z. T., & Stone, J. O. (2014). Glacial Erosion Rates from Bayesian Inversion of Cosmogenic Nuclide Concentrations in a Bedrock Core, Streaked Mtn., ME. In *American Geophysical Union Fall Meeting*. https://doi.org/Abstract ID: EP53A-3627

Rand, C., & Goehring, B. M. (2019). The distribution and magnitude of subglacial erosion on millennial timescales at Engabreen, Norway. *Annals of Glaciology*, *60*(80), 73–81. https://doi.org/10.1017/aog.2019.42

Riihimaki, C. A. (2005). Sediment evacuation and glacial erosion rates at a small alpine glacier. *Journal of Geophysical Research*, *110*(F3), F03003. https://doi.org/10.1029/2004JF000189

Schaefer, J. M., Denton, G. H., Kaplan, M., Putnam, A., Finkel, R. C., Barrell, D. J. A., et al. (2009). High-Frequency Holocene Glacier Fluctuations in New Zealand Differ from the Northern Signature. *Science*, *324*(5927), 622–625. https://doi.org/10.1126/science.1169312

Schaefer, Joerg M., Finkel, R. C., Balco, G., Alley, R. B., Caffee, M. W., Briner, J. P., et al. (2016). Greenland was nearly ice-free for extended periods during the Pleistocene. *Nature*, *540*(7632), 252–255. https://doi.org/10.1038/nature20146

Skov, D. S., Andersen, J. L., Olsen, J., Jacobsen, B. H., Knudsen, M. F., Jansen, J. D., et al. (2020). Constraints from cosmogenic nuclides on the glaciation and erosion history of Dove Bugt, northeast Greenland. *GSA Bulletin*, *132*(11–12), 2282–2294. https://doi.org/10.1130/B35410.1

Stone, J. O. (2000). Air pressure and cosmogenic isotope production. *Journal of Geophysical Research: Solid Earth*, *105*(B10), 23753–23759. https://doi.org/10.1029/2000JB900181

Strunk, A., Knudsen, M. F., Egholm, D. L., Jansen, J. D., Levy, L. B., Jacobsen, B. H., & Larsen, N. K. (2017). One million years of glaciation and denudation history in west Greenland. *Nature Communications*, *8*(1), 14199. https://doi.org/10.1038/ncomms14199

Sugden, D. E. (1978). Glacial Erosion by the Laurentide Ice Sheet. *Journal of Glaciology*, *20*(83), 367–391. https://doi.org/10.3189/S0022143000013915

Syvitski, J. P. M., Andrews, J. T., & Dowdeswell, J. A. (1996). Sediment deposition in an iceberg-dominated glacimarine environment, East Greenland: basin fill implications. *Global and Planetary Change*, *12*(1–4), 251–270. https://doi.org/10.1016/0921-8181(95)00023-2

Weidick, A. (1968). *Observations on some Holocene glacier fluctuations in West Greenland* (Vol. 165). Reitzel.

Weidick, A., & Bennike, O. (2007). Quaternary glaciation history and glaciology of Jakobshavn Isbræ and the Disko Bugt region, West Greenland: a review. *Geological Survey of Denmark and Greenland (GEUS) Bulletin*, *14*, 1–78. https://doi.org/10.34194/geusb.v14.4985

Weidick, A., Oerter, H., Reeh, N., Thomsen, H. H., & Thorning, L. (1990). The recession of the Inland Ice margin during the Holocene climatic optimum in the Jakobshavn Isfjord area of West Greenland. *Global and Planetary Change*, *2*(3), 389–399. https://doi.org/10.1016/0921-8181(90)90010-A

Willenbring, J. K., & Jerolmack, D. J. (2016). The null hypothesis: globally steady rates of erosion, weathering fluxes and shelf sediment accumulation during Late Cenozoic mountain uplift and glaciation. *Terra Nova*, *28*(1), 11–18. https://doi.org/10.1111/ter.12185

Wilson, D. S., Jamieson, S., Barrett, P., Leitchenkov, G., Gohl, K., & Larter, R. (2012). Antarctic topography at the Eocene Oligocene boundary. *Palaeogeography, Palaeoclimatology, Palaeoecology*, *335*, 24–34.

Young, N., Briner, J. P., Rood, D. H., Finkel, R. C., Corbett, L. B., & Bierman, P. R. (2013). Age of the Fjord Stade moraines in the Disko Bugt region, western Greenland, and the 9.3 and 8.2 ka cooling events. *Quaternary Science Reviews*, *60*, 76–90. https://doi.org/10.1016/j.quascirev.2012.09.028

Young, N. E., Briner, J. P., Stewart, H. A. M., Axford, Y., Csatho, B., Rood, D. H., & Finkel, R. C. (2011). Response of Jakobshavn Isbrae, Greenland, to Holocene climate change. *Geology*, *39*(2), 131–134. https://doi.org/10.1130/G31399.1

Young, Nicolá. E., Schaefer, J. M., Briner, J. P., & Goehring, B. M. (2013). A ^{10}Be production-rate calibration for the Arctic: A ^{10}BE PRODUCTION-RATE CALIBRATION FOR THE ARCTIC. *Journal of Quaternary Science*, *28*(5), 515–526. https://doi.org/10.1002/jqs.2642

Young, Nicolás E., Briner, J. P., Maurer, J., & Schaefer, J. M. (2016). ^{10}Be measurements in bedrock constrain erosion beneath the Greenland Ice Sheet margin. *Geophysical Research Letters*, *43*(22). https://doi.org/10.1002/2016GL070258

Young, Nicolás E., Lesnek, A. J., Cuzzone, J. K., Briner, J. P., Badgeley, J. A., Balter-Kennedy, A., et al. (2021). In situ cosmogenic 10Be–14C–26Al measurements from recently deglaciated bedrock as a new tool to decipher changes in Greenland Ice Sheet size. *Climate of the Past*, *17*(1), 419–450. https://doi.org/10.5194/cp-17-419-2021